Chapter 10
Piezoelectric Positioning Systems and Motors

As already stated, piezoelectric elements (in particular piezoceramic elements) enable an efficient conversion of electrical energy into mechanical energy. They provide high mechanical forces and a high dynamic performance. Piezoelectric elements are, moreover, nonwearing and feature a high rigidity. On those grounds, such elements should be ideally suited as active components in various drives. In this chapter, we will concentrate on piezoelectric positioning systems and motors. Such devices contain piezoelectric actuators, which consist of one or more piezoelectric elements. Figure 10.1 illustrates four different actuator structures that are often employed, namely (a) piezoelectric stack actuators, (b) piezoelectric bimorph actuators, (c) piezoelectric trimorph actuators, and (d) the so-called macrofiber composite (MFC [25]) actuators. While piezoelectric stack actuators comprise several piezoelectric elements being stacked, bimorph and trimorph actuators contain only two piezoelectric bars (cf. Fig. 7.27 on p. 300). In contrast to bimorph actuators, trimorph actuators are equipped with a thick metallic layer between the piezoelectric bars. MFC actuators belong to the group of piezoelectric composite transducers (see Sect. 7.4.3), which contain either thin piezoceramic plates or a large number of stripes or fibers that are skillfully contacted. To obtain robust as well as mechanically flexible devices, the active components (i.e., the piezoelectric elements) of the piezoelectric composite transducers are commonly surrounded by appropriate passive materials, e.g., polymers [22]. Not surprisingly, piezoelectric composite transducers are not restricted to actuator applications but can also be used as sensors.

Apart from their structure, the considered actuators in Fig. 10.1 differ significantly in the achievable mechanical forces and displacements in working direction, e.g., [20, 25]. Basically, we always have to choose a compromise between force and displacement; i.e., a piezoelectric actuator features either high forces or large displacements. For instance, the stacking of several elements in case of piezoelectric stack actuators yields high forces in working direction. The available displacements are, however, small in comparison with the tip displacements of piezoelectric bimorph and trimorph actuators. As a matter of fact, the large displacement of bimorph and

S. J. Rupitsch, *Piezoelectric Sensors and Actuators*, Topics in Mining, Metallurgy and Materials Engineering, https://doi.org/10.1007/978-3-662-57534-5_10

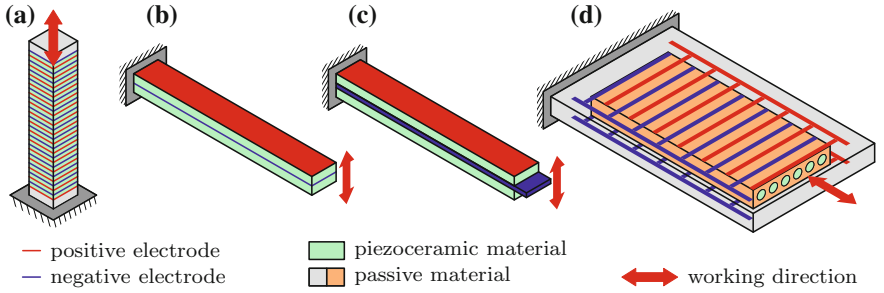

Fig. 10.1 Typical piezoelectric actuator structures for positioning systems and motors; **a** piezoelectric stack actuator; **b** piezoelectric bimorph actuator; **c** piezoelectric trimorph actuator; **d** macrofiber composite (MFC) actuator

trimorph actuators is achieved at the expense of the reachable force and rigidity. This also applies to MFC actuators.

The chapter starts with the fundamentals of piezoelectric stack actuators as well as the effect of mechanical prestress on the stack performance. Preisach hysteresis modeling from Chap. 6 will be applied to describe the large-signal behavior of prestressed stack actuators. Section 10.2 deals with so-called amplified piezoelectric actuators, which provide relatively large mechanical displacements by converting mechanical forces into displacements. The conversion is performed with the aid of special metallic hinged frames. In Sect. 10.3, the applicability of piezoelectric trimorph actuators for positioning tasks will be demonstrated. For this purpose, model-based hysteresis compensation is conducted. At the end of the chapter, a brief overview of piezoelectric motors will be given which includes selected examples of linear as well as rotary motors.

10.1 Piezoelectric Stack Actuators

Piezoelectric stack actuators are often utilized in practical applications because these actuators enable much larger strokes than single piezoelectric elements. The section starts with the fundamentals of piezoelectric stack actuators as well as typical setups. Since piezoelectric stack actuators should be mechanically prestressed in practical applications, we will take a closer look at effects of such prestress on the resulting electrical and mechanical quantities in Sect. 10.1.2. Moreover, Preisach hysteresis modeling is exploited to predict the electrical as well as mechanical large-signal behavior of a stack actuator in case of prestress.

10.1.1 Fundamentals

Actuators that are based on piezoceramic materials provide an efficient conversion of electrical energy into mechanical energy and large operating frequencies. However,

the achieved deflections of such materials for common excitation voltages are rather small. With a view to increasing the available stroke of a piezoelectric device for practical applications, it makes sense to stack several piezoceramic elements. The resulting piezoelectric device is usually termed piezoelectric stack actuator (PSA). Depending on the operating direction, we can distinguish between longitudinal PSAs and shear PSAs [6]. While longitudinal PSAs exploit the longitudinal mode of piezoelectricity (i.e., the d_{33}-effect), shear PSAs are often based on the transverse shear mode of piezoelectricity (i.e., the d_{15}-effect).

Figure 10.2a illustrates the conventional setup of a longitudinal PSA, which consists of a large number of polarized piezoceramic disks that are equipped with two electrodes each, i.e., a positive and a negative electrode. The electric polarization **P** of the piezoceramic disks points from the positive to the negative electrode. As a matter of fact, the PSA demands an electrical link of all positive electrodes and all negative electrodes, respectively. We can reduce the resulting wiring effort by stacking the disks appropriately. This means that either the positive or the negative electrode of two neighboring disks should border on each other. If a conductive adhesive is used for connecting the disks, the wiring effort will then be minimal. The manufacturing costs of such longitudinal PSAs are, however, extremely high because they have to be handmade [24]. Therefore, the conventional setup is only occasionally utilized in practical applications.

The so-called *multilayer stack actuators* (see Fig. 10.2b) represent an alternative to the conventional setup of longitudinal PSAs [8]. They can be fabricated in large numbers by a multistage manufacturing process starting with an unfired layer of the piezoceramic material. The typical layer thickness amounts 50–100 µm. By means of screen printing, the piezoceramic layer gets equipped with a thin metallic film, which serves as inner electrode of the multilayer stack actuator. Commonly, more than 100 piezoceramic layers including the printed electrodes are laminated to a block. This is done at elevated temperature and under a certain mechanical stress. During the subsequent process steps, the multilayer block is tailored, fired, and sintered just as in case of piezoceramic single elements. The block is, moreover, equipped with external

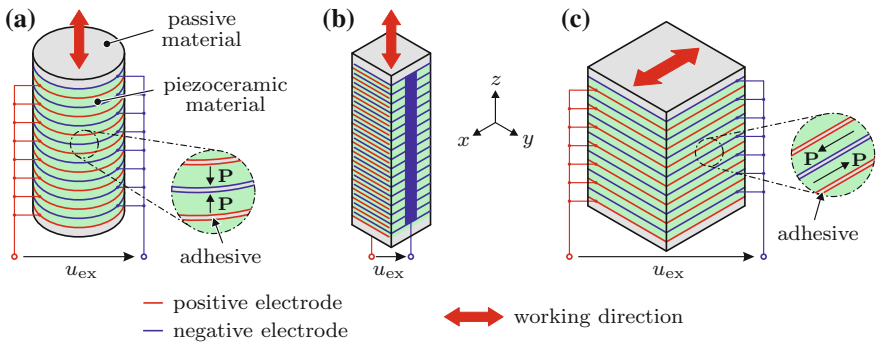

Fig. 10.2 Principle setup of **a** conventional longitudinal PSAs, **b** multilayer stack actuators, and **c** shear PSAs; **P** indicates direction of electric polarization

electrodes, which connect the inner electrodes in an appropriate manner. Finally, the multilayer stack actuator has to be polarized with a view to activating piezoelectric coupling. Such stack actuators are used in high-speed switching applications (e.g., injection system in diesel engines [6]) as well as for precision positioning.

Besides of longitudinal PSAs, one can also fabricate shear PSAs. In contrast to longitudinal PSAs, it is, however, hardly possible to build up a multilayer stack actuator because the required direction of electric polarization cannot be created by the inner electrodes. That is the reason why shear PSAs comprise individual piezoceramic elements, which are equipped with a positive and a negative electrode. Again, the wiring effort can be minimized by a conductive adhesive and an appropriate element stacking. Figure 10.2c depicts a shear PSA consisting of piezoceramic elements, which are alternately polarized in positive and negative x-direction. Therefore, the shear PSA provides comparatively large displacements between its lower and upper end in this direction. If we additionally utilize a shear PSA that contains piezoceramic elements being alternately polarized in positive and negative y-direction, a PSA combination will be achieved which allows displacements in both directions, i.e., in x- and in y-direction. For instance, such shear PSA combinations can be used in scanning microscopes. There also exists an alternative design of shear PSAs, the so-called multilayer pseudo-shear actuator, which exploits the transverse mode of piezoelectricity, i.e., the d_{31}-effect [31]. By alternately using a stiff conductive adhesive at the left and right end of the piezoceramic plates, the overall block behaves like a shear PSA.

To demonstrate the general operation principle of piezoelectric stack actuators, let us assume a mechanically unloaded (i.e., $T_3 = 0$) longitudinal PSA consisting of $n_{\text{disk}} = 100$ cylindrical piezoceramic disks. Each disk shall feature the diameter $d_S = 10\,\text{mm}$ and thickness $t_S = 0.5\,\text{mm}$. By neglecting the adhesive layer between the disks, the stack exhibits, thus, the overall length $l_{\text{stack}} = n_{\text{disk}} \cdot t_S = 50\,\text{mm}$. Furthermore, we assume a typical piezoelectric strain constant $d_{33} = 4 \cdot 10^{-10}\,\text{m V}^{-1}$ of a piezoceramic material, an excitation voltage of $u_{\text{ex;stack}} = 500\,\text{V}$, and purely linear material behavior. The assumptions lead to the mechanical strains of piezoelectric disk $S_{3;\text{disk}}$ and stack $S_{3;\text{stack}}$

$$S_{3;\text{disk}} = S_{3;\text{stack}} = d_{33} E_3 = d_{33} \frac{u_{\text{ex;stack}}}{t_S} = 4 \cdot 10^{-4} \tag{10.1}$$

in 3-direction. Therefore, the longitudinal PSA offers a stroke of

$$z_{\text{stroke}} = S_{3;\text{stack}} \cdot l_{\text{stack}} = n_{\text{disk}} \cdot S_{3;\text{disk}} \cdot t_S = 20\,\mu\text{m}\,. \tag{10.2}$$

If a piezoceramic cylinder of the same length is used instead (i.e., cylinder length $l_S = 50\,\text{mm}$), such stroke will require the excitation voltage

$$u_{\text{ex;cylinder}} = \frac{S_{3;\text{cylinder}} \cdot l_S}{d_{33}} = \frac{z_{\text{stroke}}}{d_{33}} = 50\,\text{kV}\,, \tag{10.3}$$

which is n_{disk} times higher than the excitation voltage $u_{\text{ex;stack}}$ of a stack actuator with the same performance, i.e., $u_{\text{ex;cylinder}} = n_{\text{disk}} \cdot u_{\text{ex;stack}}$. When we increase the number n_{disk} of piezoceramic disks and reduce their thickness t_{S} accordingly that the stack length l_{stack} stays constant, the obtained stroke will be improved further. This simple example already reveals the great advantage of piezoelectric stack actuators. However, one also has to consider that a stack actuator behaves electrically like the parallel connection of n_{disk} single piezoceramic disks. The capacitance C_{disk} of a single disk is given by

$$C_{\text{disk}} = \frac{\varepsilon_{33}^{T} A_{\text{S}}}{t_{\text{S}}} = \frac{\varepsilon_{33}^{T} d_{\text{S}}^{2} \pi}{4 t_{\text{S}}} \tag{10.4}$$

with the electric permittivity ε_{33}^{T} for constant mechanical stress. Therewith, the total capacitance C_{stack} of the longitudinal PSA results in

$$C_{\text{stack}} = n_{\text{disk}} \cdot C_{\text{disk}} = \frac{n_{\text{disk}} \varepsilon_{33}^{T} d_{\text{S}}^{2} \pi}{4 t_{\text{S}}} = \frac{n_{\text{disk}}^{2} \varepsilon_{33}^{T} d_{\text{S}}^{2} \pi}{4 l_{\text{stack}}} \,. \tag{10.5}$$

Compared to the capacitance $C_{\text{cylinder}} = \varepsilon_{33}^{T} A_{\text{S}} / l_{\text{stack}}$ of the piezoceramic cylinder with the same geometric dimensions, C_{stack} takes values that are n_{disk}^{2} times as large, i.e., $C_{\text{stack}} = n_{\text{disk}}^{2} \cdot C_{\text{cylinder}}$. Although the excitation voltage $u_{\text{ex;stack}}$ is relatively small, the parallel connection of n_{disk} capacitances C_{disk} increases the current consumption of the PSA remarkably. If the electric current of a single disk is i_{disk}, the current i_{stack} of the entire stack becomes $i_{\text{stack}} = n_{\text{disk}} \cdot i_{\text{disk}}$. It seems only natural that both the increasing total capacitance and the increasing current consumption have to be taken into account when designing the control electronics for a PSA.

With regard to practical applications, one should always bear in mind that PSAs are very sensitive to tensile forces. On the one hand, this is due to the adhesive layer between the piezoceramic elements in conventional setups. On the other hand, piezoceramic materials itself should generally not be loaded with tensile forces because these materials exhibit low tensile strength. Hence, tensile forces cannot only damage conventional PSAs but also multilayer stack actuators. Even if there do not act external tensile forces on the PSA, the inner forces in case of electrical excitation may cause damages. That is the reason why PSAs (especially longitudinal PSAs) are commonly mechanically prestressed in practical applications [6]. For the longitudinal PSAs in Fig. 10.2a and b, mechanical prestress means a mechanical force acting in negative z-direction on the top end, i.e., parallel to the working direction. We can generate the required prestress either with the aid of a suitable PSA housing or through an external preloading.

The permitted range of the excitation voltage u_{ex} represents a further important point concerning the practical application of PSAs. In order to avoid partial or full depolarization of the involved piezoceramic materials, PSA must not be excited by large negative voltages. To some extent, the permitted range is exclusively limited to positive voltages, i.e., $u_{\text{ex}} \geq 0\,\text{V}$. Exceptions to this are shear PSAs, which can usually be operated symmetrically around zero up to a few hundred volts. The permitted voltage range for conventional longitudinal PSAs often goes up to $u_{\text{ex}} = +1000\,\text{V}$.

The company PI Ceramic GmbH [20] is a well-known manufacturer of longitudinal and shear PSAs. Depending on the stack length l_{stack}, commercially available longitudinal PSAs in the conventional setup provide strokes of more than 30 µm. The blocking forces can reach values >50 kN in longitudinal direction. Note that the blocking force will correspond to the maximum mechanical force when actuator displacements are completely prevented. Multilayer stack actuators allow strokes >30 µm and blocking forces greater than 3000 N. The maximum displacement of commercially available shear PSAs typically amounts 10 µm. However, due to the setup of shear PSAs, the permitted maximum of the shear load hardly exceeds 200 N.

10.1.2 Effect of Mechanical Prestress on Stack Performance

Figure 10.3 depicts the investigated longitudinal piezoelectric stack actuator PICA P-010.20P of cylindrical shape, which was manufactured by the company PI Ceramic GmbH [20]. The PSA consists of $n_{\text{disk}} = 50$ single disks made of the ferroelectrically soft material PIC255. Owing to the fact that the disks are polarized and stacked in 3-direction, the stack actuator mainly elongates in 3-direction, which also represents the working direction. Consequently, it makes sense to restrict the further investigations to the 3-direction. This includes the decisive physical quantities (e.g., mechanical strain), which means that we consider solely their 3-components. The most important specifications of the PSA are listed in Table 10.1.

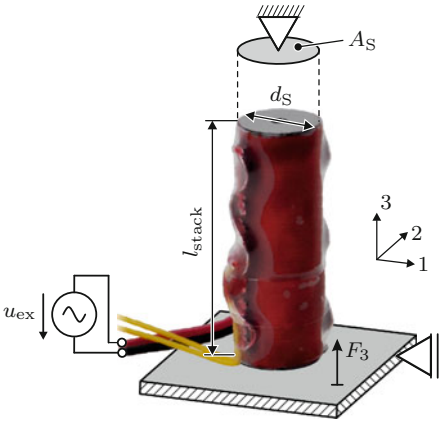

Fig. 10.3 Piezoelectric stack actuator PICA P-010.20P manufactured by PI Ceramic GmbH; total length l_{stack} and cross section $A_S = d_S^2\pi/4$; electrical excitation u_{ex}; applied mechanical prestress $T_3 = F_3/A_{\text{disk}}$

Table 10.1 Specifications of investigated longitudinal piezoelectric stack actuator PICA P-010.20P

Thickness t_S of a single disk	≈0.5 mm
Diameter d_S of a single disk	10 mm
Disk material	PIC255
Amount n_{disk} of single disks	50
Total length l_{stack} of the stack actuator	31 mm
Maximum permissible mechanical prestress $T_{3;max}$	30 MPa
Electrical excitation voltage u_{ex}	0 . . . 1 kV

Let us start with the maximum achievable values for both the electric polarization P^+_{max} and the mechanical strain[1] S^+_{max} of the PSA in the unipolar working area (see Fig. 6.1 on p. 196) state of the actuator is unknown, we will exclusively quantify maximum changes of those quantities, i.e., ΔP^+_{max} and ΔS^+_{max}. Just as in Chap. 6, a Sawyer–Tower circuit and a linear variable differential transformer were utilized to acquire ΔP and ΔS, respectively. The PSA was exposed to a mechanical prestress $T_3 = F_3/A_{disk}$ in thickness direction through a tension–compression testing machine. Firstly, T_3 was stepwise increased from 0 MPa to 30 MPa in steps of 2.5 MPa and, secondly, stepwise reduced again to the mechanically unloaded case (i.e., $T_3 = 0$ MPa). In order to ensure that all transient phenomena within the actuator have decayed, the electrical excitation was applied after a waiting time of 5 min. The sinusoidal excitation voltage (frequency $f = 0.1$ Hz) featured an amplitude of $\hat{u}_{ex} = 500$ V and an offset of $U_{off} = +500$ V; i.e., the PSA was operated in the permissible range (see Table 10.1). This leads to the maximum electric field intensity $E = 2\,\mathrm{kV\,mm^{-1}}$ within a single disk.

Figure 10.4a and b show the obtained results for ΔP^+_{max} and ΔS^+_{max} of the PSA with respect to $T_3^{\pm}$. Interestingly, both quantities rise with increasing mechanical prestress T_3^+ and drop with decreasing prestress T_3^- in the investigated value range. Such behavior is mainly attributable to the fact that several domains within the ferroelectric material switch to the ferroelastic intermediate stage due to applied prestresses [34]. As a consequence, the global electric polarization of the PSA reduces, but the amount of domains that can be aligned in parallel to the applied electric field increases. Therefore, the changes of electric polarizations ΔP^+_{max} and mechanical strains ΔS^+_{max} also rise in the considered range of mechanical prestresses (cf. Fig. 6.21c on p. 236). It has to be noted that a further increase of the prestress would, however, drastically reduce ΔP^+_{max} as well as ΔS^+_{max} since the domains stay in the ferroelastic intermediate stage. In other words, the applied electric field is no longer capable to align domains within the ferroelectric material. Besides, there occurs a certain hysteresis for increasing prestress T_3^+ and decreasing prestress T_3^- in $\Delta P^+_{max}(T_3)$ as well as $\Delta S^+_{max}(T_3)$, i.e., $\Delta P^+_{max}\left(T_3^+\right) \neq \Delta P^+_{max}\left(T_3^-\right)$ and $\Delta S^+_{max}\left(T_3^+\right) \neq \Delta S^+_{max}\left(T_3^-\right)$. The reason for this lies in altered domain configurations within the ferroelectric material for increasing and decreasing prestresses.

[1] The given mechanical strains of the PSA always relate to its total length l_{stack}.

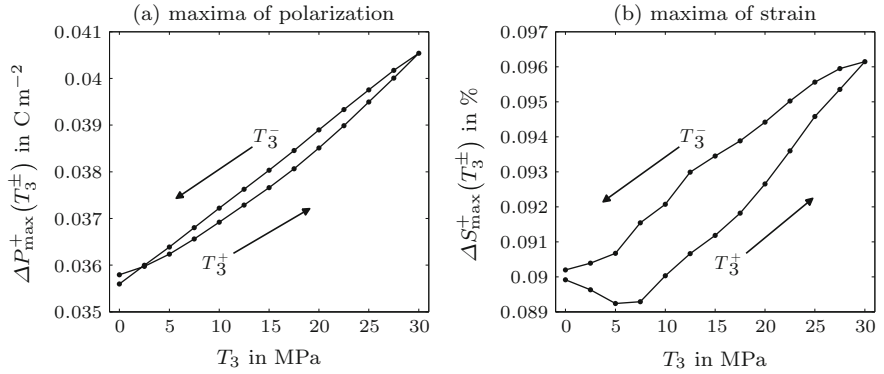

Fig. 10.4 Variation of **a** maximum electric polarization $\Delta P^{+}_{\max}(T_3)$ and **b** maximum mechanical strain $\Delta S^{+}_{\max}(T_3)$ versus applied mechanical prestress T_3; increasing prestress T_3^+ and decreasing prestress T_3^-; piezoelectric stack actuator PICA P-010.20P operating in unipolar working area

10.1.3 Preisach Hysteresis Modeling for Prestressed Stack

As the results in Fig. 10.4 demonstrate, $\Delta P^{+}_{\max}$ and $\Delta S^{+}_{\max}$ of the PSA strongly depend on the applied mechanical prestress T_3. The values (especially $\Delta P^{+}_{\max}$) are altered up to almost 15% in the investigated range of T_3. Accordingly, it seems only natural that the underlying large-signal behavior of the electric polarization and mechanical strain also varies. With a view to studying this effect more in detail, additional measurements were conducted for the actuator operating in the unipolar working area. In particular, a unipolar electrical excitation signal of sinusoidal shape was utilized which features decreasing amplitudes and a frequency of $f = 0.1$ Hz. The mechanical prestress T_3^+ was again stepwise increased from 0 MPa to 30 MPa in steps of 2.5 MPa. After a waiting time of 5 min, the PSA was excited with the unipolar electrical input sequence. Figure 10.5a and b show the collected measurements for the electric polarization $\Delta P_{\text{meas}}(t, T_3)$ and mechanical strain $\Delta S_{\text{meas}}(t, T_3)$ with respect to time t as well as applied prestress T_3. Similar to the previous experiments, the strong dependence on T_3 becomes apparent. This can also be seen in the resulting hysteresis curves $\Delta P_{\text{meas}}(E, T_3)$ and $\Delta S_{\text{meas}}(E, T_3)$ in Fig. 10.5c and d.

To incorporate the applied mechanical prestress T_3 in Preisach hysteresis modeling for the PSA, it is advisable to proceed in the same manner as in Sect. 6.6.5. This means that we introduce a weighting distribution $\mu_{\text{DAT}}(\alpha, \beta, T_3)$ for the elementary switching operators of the generalized Preisach hysteresis operator $\mathcal{H}_{\text{G}}$, which additionally depends on T_3. In a first step, the entire parameter set of $\mu_{\text{DAT}}(\alpha, \beta, T_3)$ is identified for $\Delta P(E, T_3)$ as well as $\Delta S(E, T_3)$ separately in case of the mechanically unloaded PSA, i.e., $T_3 = 0$. Subsequently, selected parameters have to be modified with respect to T_3. In contrast to the piezoceramic disk in Sect. 6.6.5, it is here sufficient to solely alter the parameter B because the considered PSA only operates in the unipolar working area. As the comparison of measured and simulated hysteresis

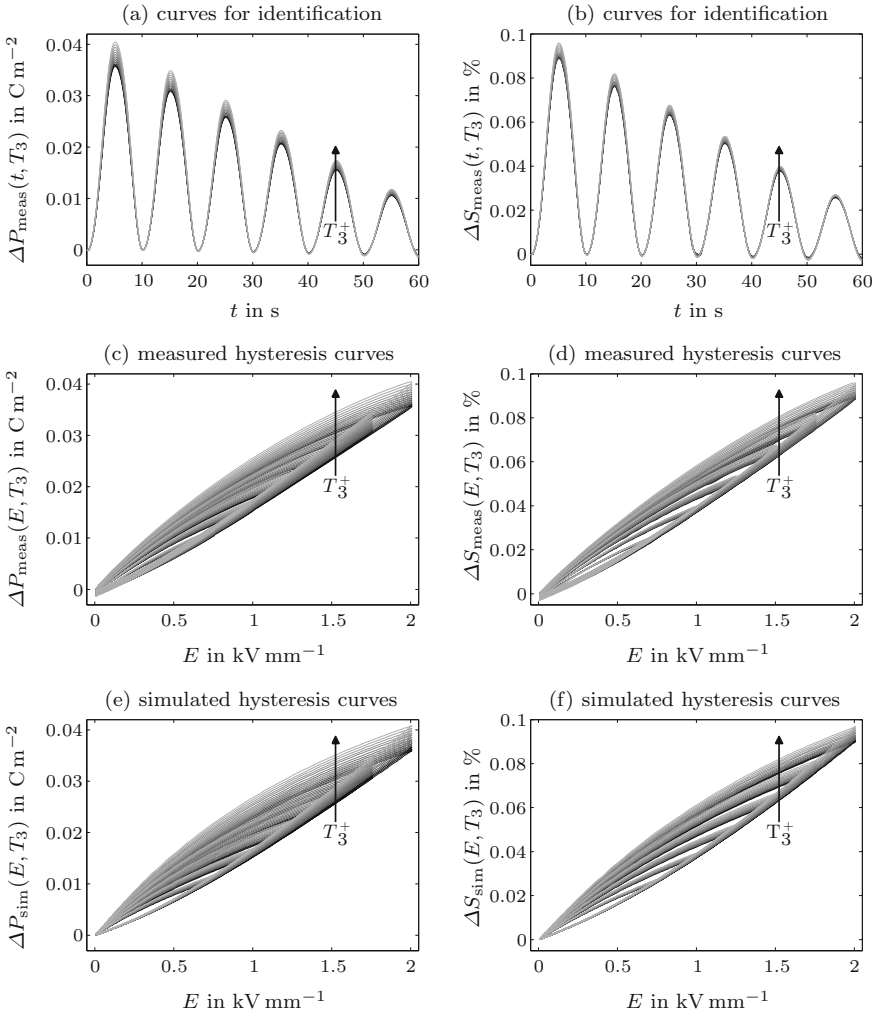

Fig. 10.5 **a** and **b** Measured curves $\Delta P_{\mathrm{meas}}(t, T_3)$ and $\Delta S_{\mathrm{meas}}(t, T_3)$ versus time t and increasing mechanical prestress T_3^+ for identifying parameters of Preisach hysteresis operator; **c** and **d** measured hysteresis curves $\Delta P_{\mathrm{meas}}(E, T_3)$ and $\Delta S_{\mathrm{meas}}(E, T_3)$; **e** and **f** simulated hysteresis curves $\Delta P_{\mathrm{sim}}(E, T_3)$ and $\Delta S_{\mathrm{sim}}(E, T_3)$; piezoelectric stack actuator PICA P-010.20P operating in unipolar working area

curves in Fig. 10.5c–f indicates, the generalized Preisach hysteresis model performs excellently. Even if the mechanical prestress changes, we will be able to realistically describe the large-signal behavior of the PSA in the unipolar working area.

The same investigations were conducted for a decreasing mechanical prestress T_3^-; i.e., T_3^- was stepwise reduced from 30 MPa to 0 MPa in steps of 2.5 MPa. Figure 10.6a and b contains the identified parameter values of $B_P(T_3)$ as well as $B_S(T_3)$ for

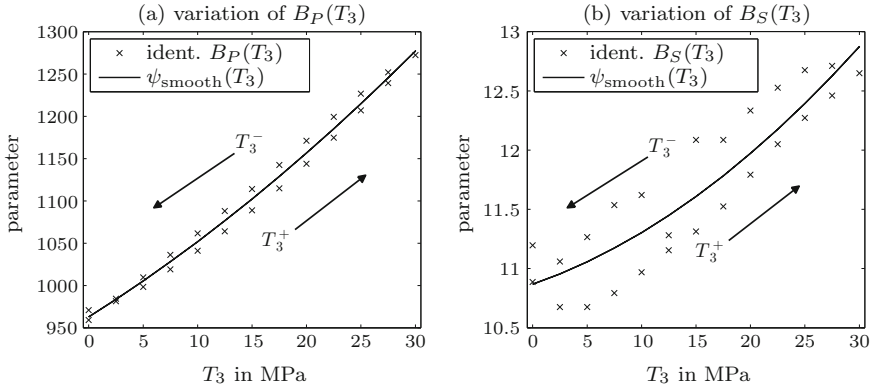

Fig. 10.6 Variation of parameter B as well as smoothing function $\psi_{\text{smooth}}(T_3)$ according to (10.6) versus applied mechanical prestress T_3 for Preisach hysteresis modeling; **a** $B_P(T_3)$ for electric polarization and **b** $B_S(T_3)$ for mechanical strain; increasing prestress T_3^+ and decreasing prestress T_3^-; piezoelectric stack actuator PICA P-010.20P operating in unipolar working area

Table 10.2 Parameters ς_i of smoothing function $\psi_{\text{smooth}}(T_3)$ in (10.6) for B_P and B_S, which are required to define weighting distribution $\mu_{\text{DAT}}(\alpha, \beta, T_3)$

		ς_1	ς_2	ς_3
Polarization	$B_P(T_3)$	962.8092	8.1108	0.0788
Strain	$B_S(T_3)$	10.8679	0.0319	0.0012

increasing and decreasing prestress, respectively. Due to smooth progression of the parameter values, they can also serve as data points of an appropriate smoothing function $\psi_{\text{smooth}}(T_3)$. Here, we use the function (cf. (6.30, p. 237))

$$\psi_{\text{smooth}}(T_3) = \varsigma_1 + \varsigma_2 \left(\frac{T_3}{1\,\text{MPa}} \right) + \varsigma_3 \left(\frac{T_3}{1\,\text{MPa}} \right)^2 . \tag{10.6}$$

The resulting values of ς_i for $B_P(T_3)$ and $B_S(T_3)$ are listed in Table 10.2.

For validation purpose, let us exploit the determined parameter set to predict polarizations and strains of the PSA for an electrical excitation signal, which was not considered during the identification procedure. Contrary to the identification signal, the unipolar excitation signal for validation features rising amplitudes. Figure 10.7a and b display the measured curves $\Delta P_{\text{meas}}(t, T_3)$ and $\Delta S_{\text{meas}}(t, T_3)$ with respect to t and T_3. The corresponding simulation results $\Delta P_{\text{sim}}(t, T_3)$ and $\Delta S_{\text{sim}}(t, T_3)$ are shown in Fig. 10.7c and d. Again, the comparison clearly points out that one is able to reliably predict the large-signal behavior of the PSA through Preisach hysteresis modeling, even in case of applied mechanical prestress. This is also confirmed by the normalized relative deviations ϵ_r between simulations and measurements, which always stay below 5% (see Fig. 10.7e and f). However, if the mechanical prestress is not taken into account, the modeling approach will yield relative deviations of more than 10% [34].

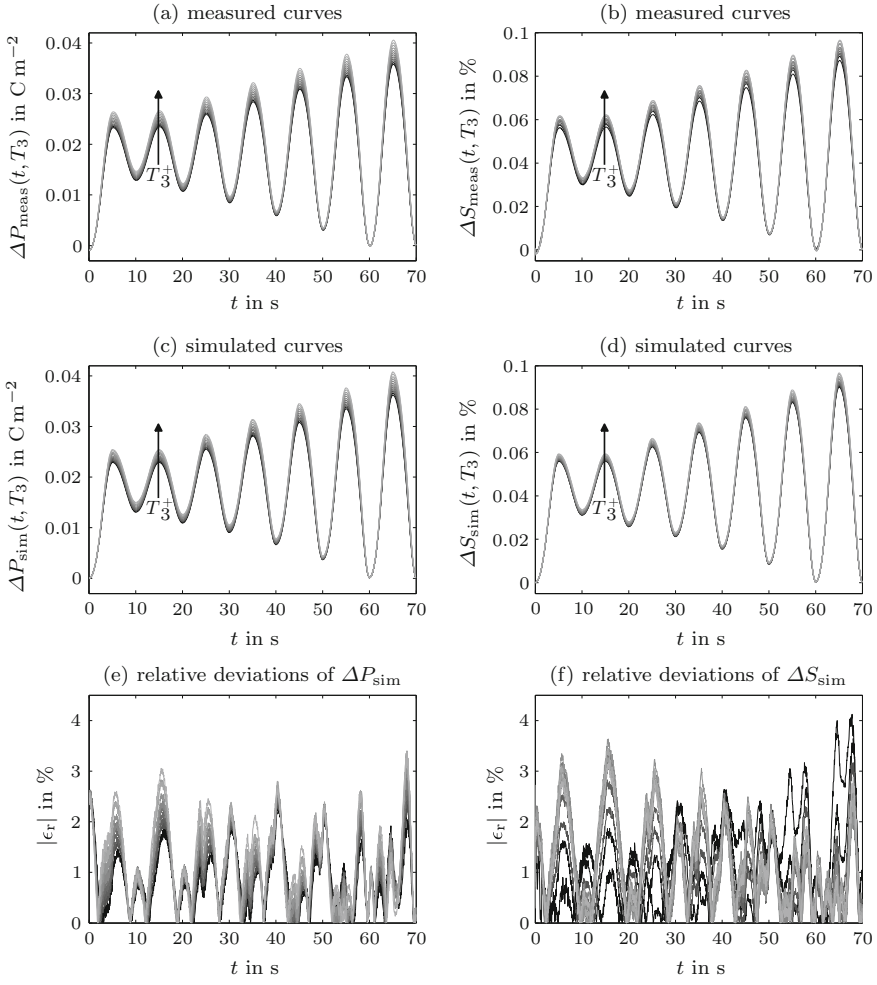

Fig. 10.7 **a** and **b** Measured curves $\Delta P_{\mathrm{meas}}(t, T_3)$ and $\Delta S_{\mathrm{meas}}(t, T_3)$ versus time t and increasing mechanical prestress T_3^+ for validating Preisach hysteresis model; **c** and **d** simulated curves $\Delta P_{\mathrm{sim}}(t, T_3)$ and $\Delta S_{\mathrm{sim}}(t, T_3)$ versus time t and increasing mechanical prestress T_3^+; **e** and **f** collected normalized relative deviations $|\epsilon_{\mathrm{r}}|$ in % (magnitude); piezoelectric stack actuator PICA P-010.20P operating in unipolar working area

10.2 Amplified Piezoelectric Actuators

Even though piezoelectric stack actuators provide huge blocking forces, excellent positioning accuracy as well as large operating frequencies, the available strokes are much smaller than those of electromagnetic actuators. This fact constitutes a considerable disadvantage for various practical applications like vibration sources. The

so-called amplified piezoelectric actuators (APA) supply remedy because they provide large strokes by converting mechanical forces into displacements. The working principle and basic design of an APA will be explained in Sect. 10.2.1. Subsequently, we will discuss simulation results, which allow to deduce design criteria for amplified piezoelectric actuators. In Sect. 10.2.3, experimental results for different APA configurations will be compared to corresponding simulation results.

10.2.1 Working Principle

Amplified piezoelectric actuators always consist of piezoelectric elements and appropriate structures for converting mechanical forces into displacements. In the majority of cases, piezoelectric stack actuators serve as piezoelectric elements since the available strokes of such actuators are much higher than those of single piezoelectric elements, e.g., a disk. The conversion structure contains a certain amount of arms and is often diamond-shaped, which can be achieved either by the pitch angles of straight structure arms or by arms featuring the shape of suitable free-form curves, e.g., [11, 15, 17, 38]. Apart from the structure shape, the connection of the arms greatly influences the performance of the APA.

Figure 10.8a shows the typical setup of an APA containing a PSA and a metallic hinged frame for conversion. The hinged frame comprises four arms with two joints each. If the PSA expands due to electrical excitation, a mechanical force will be introduced to the hinged frame and its geometric dimension in x-direction will increase. This goes hand in hand with a reduction of the frame dimensions in y-direction. As a matter of fact, the geometric changes depend on the excitation signal, the geometric circumstances of stack actuator and frame as well as on their material properties.

In a first step, let us conduct a purely geometric consideration of the APA in Fig. 10.8a. Therefore, we assume ideal hinges and neglect acting forces as well as material properties. The symmetrical hinged frame comprising four nondeformable arms can then be reduced to a single arm of constant length l_A [14, 15]. While the left-end P_L of the arm moves only in y-direction, the right-end P_R moves only in

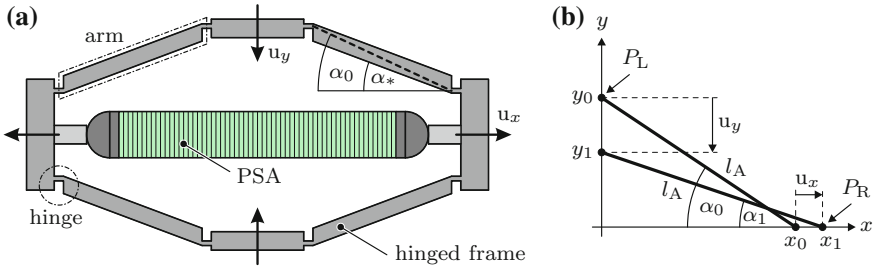

Fig. 10.8 **a** Typical setup of APA containing piezoelectric stack actuator (PSA) and closed hinged frame with four arms; **b** quantities for geometric consideration of single APA arm

x-direction. Figure 10.8b depicts the geometric circumstances for the initial state (i.e., without actuator excitation) and for the expanded state. In the initial and expanded state, the end positions of the arm are given by (x_0, y_0) and (x_1, y_1), respectively. The resulting effective pitch angles of the arm read as

$$\alpha_0 = \arctan\left(\frac{y_0}{x_0}\right) \quad \text{and} \quad \alpha_1 = \arctan\left(\frac{y_1}{x_1}\right) . \tag{10.7}$$

Owing to the fact that l_A is assumed to remain constant, both states have to satisfy

$$l_\mathrm{A} = \sqrt{x_0^2 + y_0^2} = \sqrt{x_1^2 + y_1^2} = \sqrt{(x_0 + \mathrm{u}_x)^2 + \left(y_0 + \mathrm{u}_y\right)^2} \tag{10.8}$$

with the displacement u_x of P_R in positive x-direction and u_y of P_L in positive y-direction. By solving for u_y, which represents the aimed quantity, (10.8) becomes

$$\begin{aligned} \mathrm{u}_y &= -y_0 \pm \sqrt{y_0^2 - \mathrm{u}_x^2 - 2x_0\mathrm{u}_x} \\ &= -l_\mathrm{A} \sin\alpha_0 + \sqrt{(l_\mathrm{A} \sin\alpha_0)^2 - \mathrm{u}_x^2 - 2l_\mathrm{A} \cos\alpha_0 \mathrm{u}_x} . \end{aligned} \tag{10.9}$$

This means that the displacement u_y of the hinged frame in y-direction depends exclusively on the actuator stroke u_x, the arm length l_A, and the pitch angle α_0 in the initial state. Because we modeled a quarter of the setup, u_x and u_y denote half of the actuator stroke and half of the entire frame displacement, respectively. It seems only natural that an APA should fulfill the condition $\mathrm{u}_y > \mathrm{u}_x$.

10.2.2 Numerical Simulations for Parameter Studies

The geometric considerations in the previous subsection neglect both the acting forces and the material properties of the APA components. It is not surprising that such an approach represents an oversimplification of the actual circumstances. To describe the behavior of an APA in a reliable way, we need, therefore, alternative three-dimensional approaches like elastostatic modeling, compliance-based modeling, or finite element (FE) analysis [13]. In the context of elastostatic modeling, the support reactions (i.e., forces and torques) at P_L and P_R are evaluated as function of the acting forces. These forces are given by the generated force of the PSA and the weight forces. The combination of support reactions and strain energy yields the displacements u_x and u_y of the APA. In case of compliance-based modeling, one has to introduce an elastic compliance tensor $[\mathbf{s}]$ for each component of the APA, i.e., for the structure arms and the PSA. From the acting forces and the resulting compliance tensor of the APA, we are again able to compute u_x as well as u_y. Although the elastostatic and compliance-based modeling approaches are rather simple, they exhibit serious weaknesses. Both modeling approaches do not allow to determine eigenfrequencies

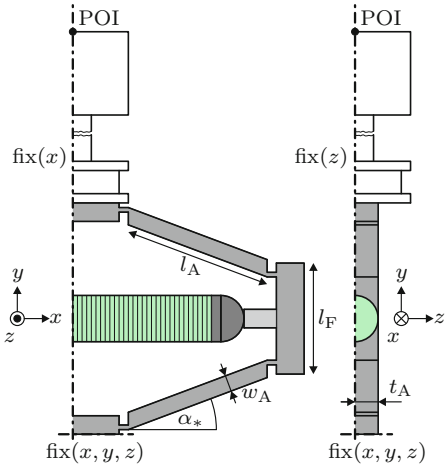

Fig. 10.9 Schematic front and side view of three-dimensional FE model of APA with sample holder [14]; FE model represents quarter of overall structure; point of interest (POI); geometric pitch angle α_* of arm

of the APA, which are of utmost importance concerning practical applications [14]. Moreover, the underlying calculation procedures require the acting force of the PSA. On these grounds, we will exclusively focus on the FE method hereinafter. In contrast to elastostatic and compliance-based modeling, the FE method can be used for several types of analysis, e.g., eigenfrequency analysis. The consideration of piezoelectric coupling (see Sect. 4.5.1) also enables the determination of u_x and u_y for a given electrical excitation of the PSA.

Figure 10.9 depicts a schematic front and side view of the three-dimensional FE model including characteristic geometric dimensions. The FE model was created according to the APA configurations that were built up at the Chair of Sensor Technology (Friedrich-Alexander-University Erlangen-Nuremberg). Besides of the PSA and the metallic hinged frame, the simulation model contains a sample holder made of acrylic glass. Owing to its symmetry, the entire setup can be reduced to a quarter, which remarkably reduces to computation effort and makes certain boundary conditions for the mechanical displacement necessary. The boundary conditions $\mathrm{fix}(x)$ and $\mathrm{fix}(z)$ imply that the displacements are zero in x- and z-direction, respectively. Because the ground plate of the realized APA is fixed, the FE model contains additionally $\mathrm{fix}(x, y, z)$ at its bottom.

The cylindrically shaped piezoelectric stack actuator P-010.40P from the company PI Ceramic GmbH [20] serves as piezoelectric element in the realized setup. The stack with diameter $d_S = 10$ mm and total length $l_{\mathrm{stack}} = 58$ mm consists of 98 active disks that are made of the ferroelectrically soft material PIC255. They are equipped with electrodes and glued together. At the bottom and top end, the stack contains a ceramic plate as well as a steel plate.The active disks are alternately polarized

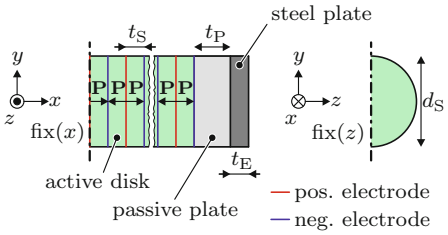

Fig. 10.10 Schematic front and side view of three-dimensional FE model of PSA [14]; FE model represents quarter of overall structure; **P** indicates direction of electric polarization

Table 10.3 Numbers and geometric dimensions of components for FE model of PSA in Fig. 10.10

	Number	Geometric dimensions
Passive ceramic plate	1	Thickness $t_P = 1.0$ mm
Active piezoelectric disk	49	Thickness $t_S = 0.56$ mm
Steel plate	1	Thickness $t_E = 0.5$ mm

in opposite directions. Figure 10.10 illustrates a schematic front and side view of the PSA in the FE model. Table 10.3 summarizes the number of components and geometric dimensions. Note that the adhesive layers and electrodes between the disks were not considered in the simulation. The material parameters of PIC255 were taken from the results of the inverse method in Table 5.3 on p. 160. For the metallic hinged frame that is made of tool steel, the decisive material parameters density, Young's modulus, and Poisson's ratio were assumed to be $\varrho_0 = 7800\,\mathrm{kg\,m^{-3}}$, $E_M = 210\,\mathrm{GPa}$, and $\nu_P = 0.28$.

As already mentioned, the numerical simulations were conducted for different configurations of the APA [14]. While the PSA remains unchanged for all configurations, the metallic frame was altered. This refers to the hinge design and its geometric dimensions as well as to the arm length l_A. In Fig. 10.11, one can see the two types of considered hinge designs with the characteristic dimensions w_H and l_H. Type A contains rounded cuts, whereas hinges of type B feature a rectangular shape. It is not surprising that both arm length and hinge influence the effective pitch angle α_0 of the arms and, therefore, the conversion of u_x into u_y, which is provided from the APA.

Table 10.4 contains the initial parameters of the hinged frame for the harmonic FE simulations, which were carried out in frequency range from 10 Hz to 3 kHz. Let us start with simulation results for a hinge of type B. Figure 10.12 displays the normalized simulated velocity amplitude $\hat{v}_y(f) = 2\pi f \hat{u}_y(f)$ in y-direction at the point of interest (POI) that corresponds to the top end of the sample holder (cf. Fig. 10.9). The first resonance in $\hat{v}_y(f)$ occurs at a frequency of $f_r \approx 300$ Hz. Until shortly before this resonance, $\hat{v}_y(f)$ rises linearly with the frequency since the displacement amplitude $\hat{u}_y(f)$ at the POI stays almost constant. If the arm length l_A of the hinged frame is reduced (e.g., $l_A = 15$ mm), f_r will increase which might be amajor advantage. However, the available velocity amplitude below f_r will decrease

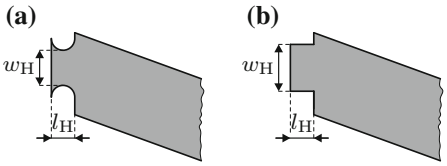

Fig. 10.11 Characteristic geometric dimensions of hinges of **a** type A and **b** type B

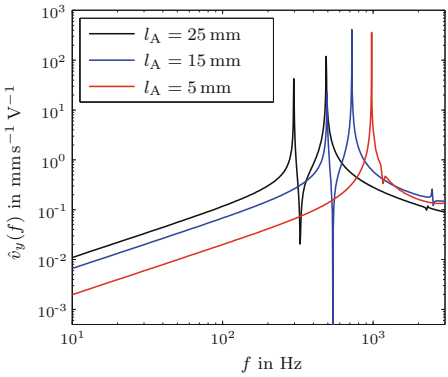

Fig. 10.12 Normalized simulated velocity amplitude $\hat{v}_y(f)$ of APA at POI for different arm lengths l_A; hinges of type B; geometric parameters listed in Table 10.4; normalization to amplitude $\hat{u}_{ex}$ of PSA excitation voltage

for shorter values of l_A. Similar studies can be performed for the other geometric parameters of the hinged frame. Table 10.4 summarizes the simulated influence of the geometric parameters on $\hat{v}_y(f)$ and f_r. Thereby, one parameter was increased, while the other parameters remain unchanged. The table entries demonstrate that similar to l_A, a larger length l_H of the hinge is accompanied by a higher $\hat{v}_y(f)$ and a lower f_r. The opposite behavior arises for the arm height w_A, the hinge height w_H, and the geometric pitch angle α_* of the arms. If these parameters are increased, $\hat{v}_y(f)$ will decrease and f_r will increase. The influence of frame thickness t_A as well as height l_F on both parameters is comparatively low. As a matter of fact, the material parameters of the PSA and the hinged frame also have a strong impact on the APA performance. Because these material parameters are predefined for the realized setup, their influence was not studied.

Guided by the parameter study, one can create different APA designs with regard to the practical application. In the present case, the APA should provide high velocities $\hat{v}_y(f)$ at the POI up to a frequency of $f = 80\,\text{Hz}$, which implies that f_r has to be much greater than 80 Hz. For this purpose, five metallic hinged frames were designed and fabricated at the Chair of Sensor Technology [14]. The closed frames (see Fig. 10.13) of constant frame thickness $2t_A = 10\,\text{mm}$ and constant arm height $w_A = 5\,\text{mm}$ differ in the geometric dimensions l_A, l_H, w_H and α_* as well as

Table 10.4 Initial geometric parameters of metallic hinged frame for FE simulations; simulated influence of individually increasing parameters on velocity amplitude $\hat{v}_y(f)$ below resonance and first resonance frequency f_r; ↑ and ↓ indicate strong increase and strong decrease, respectively; ↗ and ↘ indicate slight increase and slight decrease, respectively

Parameter	Initial value	$\hat{v}_y(f)$	f_r
l_A	25 mm	↑	↓
l_H	1 mm	↑	↓
w_A	5 mm	↓	↑
w_H	0.5 mm	↓	↑
α_*	1°	↑	↓
t_A	5 mm	↘	↗
l_F	30 mm	↘	↓

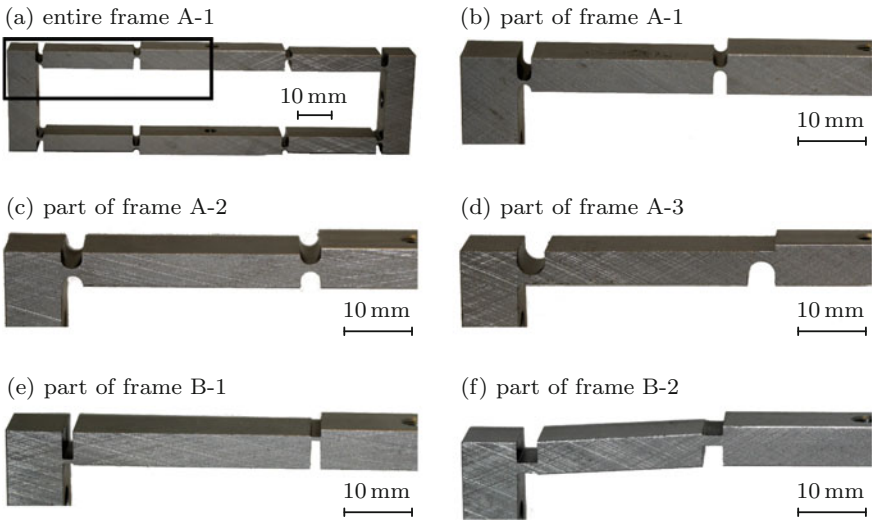

Fig. 10.13 Fabricated closed metallic frames for APA [14]; **a** entire frame A-1; part of **b** frame A-1, **c** frame A-2, **d** frame A-3, **e** frame B-1, and **f** frame B-2; decisive geometric dimensions are listed in Table 10.5

in the hinge designs. The metallic frames are designated as A-1, A-2, A-3, B-1, and B-2, whereby the letter stands for the hinge type. Table 10.5 lists the characteristic geometric dimensions of the individual frames. Figure 10.14 displays the obtained normalized simulation results of $\hat{v}_y(f)$ for the frames. To some extent, the frequency-resolved amplitudes show large differences. Due to the thin hinges of A-1 and B-1, these frames provide large velocities but exhibit small resonance frequencies. By contrast, the hinges of the frames A-2, A-3, and B-2 are stiffer which goes hand in hand with lower values of $\hat{v}_y(f)$ and higher values of f_r. In each case, f_r takes much higher values than 80 Hz. The achieved velocity amplitudes at 80 Hz and resonance frequencies are listed in Table 10.5.

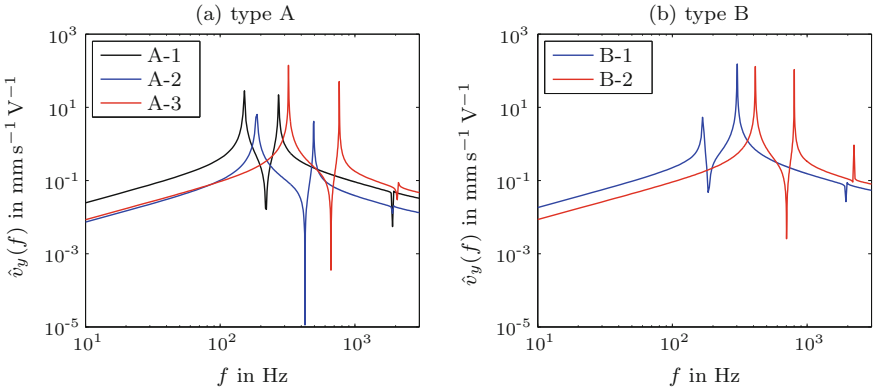

Fig. 10.14 Normalized simulated velocity amplitudes $\hat{v}_y(f)$ of APA at POI for hinges of **a** type A and **b** type B; normalization to amplitude $\hat{u}_{\mathrm{ex}}$ of PSA excitation voltage

Table 10.5 Decisive geometric dimensions of hinged frames in Fig. 10.13; simulated normalized displacement amplitudes $\hat{\mathrm{u}}_y$ and velocity amplitudes $\hat{v}_y$ of POI at 80 Hz for different frames; simulated frequency f_{r} of first resonance

Type	A-1	A-2	A-3	B-1	B-2
l_{A} in mm	26	31	29	34	24
l_{H} in mm	2.0	3.0	4.0	1.5	3.0
w_{H} in mm	0.5	1.0	1.5	0.5	1.5
α_*	0°	0°	0°	0°	3°
l_{F} in mm	30	25	25	25	26
$\hat{\mathrm{u}}_y$ in nm V^{-1}	539	147	149	338	145
$\hat{v}_y$ in µm s^{-1} V^{-1}	271	74	75	170	73
f_{r} in Hz	151	188	321	168	412

10.2.3 Experimental Verification

With a view to verifying the simulation results, measurements were conducted in addition [14]. Figure 10.15 shows the realized APA with the sample holder. At the bottom end, the APA is equipped with a rigid adapter plate made of stainless steel. The displacements amplitudes $\hat{\mathrm{u}}_y(f)$ and velocity amplitudes $\hat{v}_y(f)$ at the POI (i.e., at the top end of the sample holder) were acquired by the laser vibrometer OFV 303/3001 from the company Polytec GmbH [21]. In doing so, the PSA was excited harmonically by a sinusoidal voltage of the amplitude $\hat{u}_{\mathrm{ex}} = 1.5\,\mathrm{V}$ around the constant offset $U_{\mathrm{off}} = +1.5\,\mathrm{V}$. Therefore, the excitation voltage varied between 0 and 3 V. The frequency range of the electrical excitation was chosen according to the simulations, i.e., from 10 Hz up to 3 kHz.

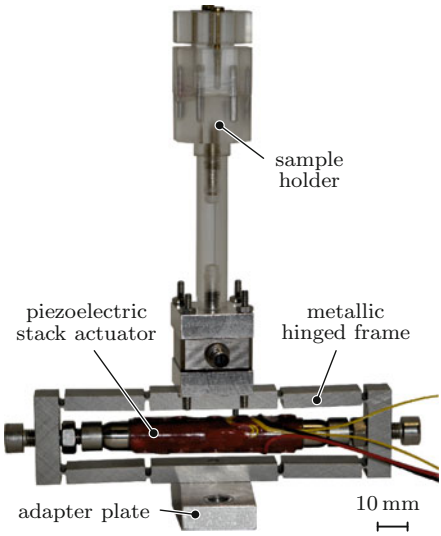

Fig. 10.15 Realized APA including piezoelectric stack actuator, closed metallic hinged frame (types A-1, A-2, A-3, B-1, or B-2), adapter plate as well as sample holder [14]

Figure 10.16a and b display the normalized measurement results of $\hat{v}_y(f)$ for the hinges of type A and type B, respectively. As the comparison with Fig. 10.14 reveals, the measurements show a similar behavior as the simulation results. This means that the frames with the hinges A-1 and B-1 provide large velocity amplitudes at $f = 80\,\mathrm{Hz}$, while the frames with the hinges A-2, A-3, and B-2 offer higher values of the resonance frequency f_r. For low excitation frequencies (i.e., $f < 40\,\mathrm{Hz}$), the measurement results should be interpreted with caution since small velocities lead to noisy output signals of the laser vibrometer.

Table 10.6 contains for each frame the measurement values for $\hat{\mathrm{u}}_y(80\,\mathrm{Hz})$, $\hat{v}_y(80\,\mathrm{Hz})$, and f_r. Although the basic behavior of simulations and measurements coincides very well, the differences in the absolute values are remarkable (cf. Table 10.5). In particular, the displacement and velocity amplitudes strongly deviate from each other. The deviations are mainly caused by three reasons. Firstly, the geometric circumstances of the metallic frames change slightly after inserting the PSA. This applies above all to the effective pitch angle α_0 of the frame arms, which influences the nonlinear relation between u_x and u_y (see (10.8)). Secondly, the conducted linear FE simulations do not consider prestresses inside PSA and hinged frame. Last but not least, the simple FE model of the stack actuator contains neither adhesive layers nor electrode layers between the almost 100 disks. Of course, both layers greatly affect the performance of the APA. It makes, however, hardly sense to take them into account since the computation effort of the FE simulations would increase remarkably. Moreover, we do not know their material behavior and geometric dimensions, in particular of the adhesive layers. A potential remedy would be a homogenized FE model of the PSA [32, 33]. Instead of the complex layer structure, the actuator would then consist of one homogeneous cylindrical-shaped material with fictive properties.

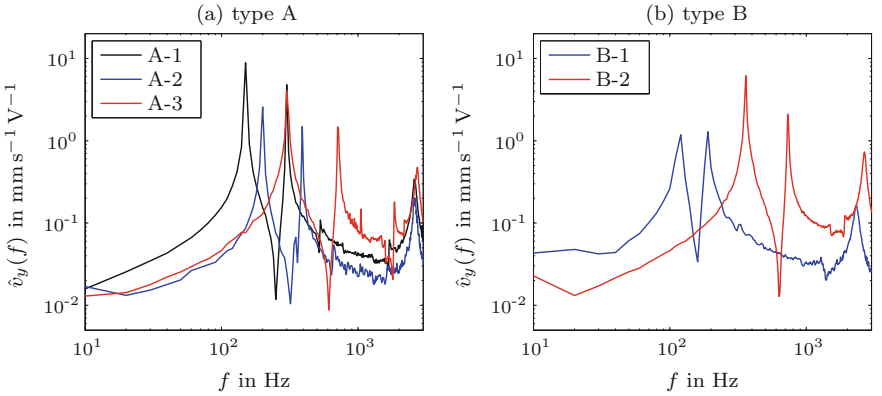

Fig. 10.16 Normalized measured velocity amplitudes $\hat{v}_y(f)$ of APA at POI for hinges of **a** type A and **b** type B; normalization to amplitude $\hat{u}_{\mathrm{ex}}$ of PSA excitation voltage

Table 10.6 Measured normalized displacement amplitudes $\hat{\mathrm{u}}_y$ and velocity amplitudes $\hat{v}_y$ of POI at 80 Hz for different frames; measured frequency f_{r} of first resonance

Type	A-1	A-2	A-3	B-1	B-2
$\hat{\mathrm{u}}_y$ in nm V^{-1}	190	55	70	237	69
$\hat{v}_y$ in μm s^{-1} V^{-1}	101	31	37	133	38
f_{r} in Hz	150	200	300	120	360

These material properties can be identified by means of the inverse method (see Sect. 5.2), i.e., by an iterative adjustment of numerical simulations to measurements.

The practical use of the APA including the sample holder calls commonly for much higher displacement and velocity amplitudes than given in Table 10.6. That is the reason why the piezoelectric stack actuator has to be excited by AC voltages with amplitudes $\hat{u}_{\mathrm{ex}} \gg 1$ V. In the present case, the experiments were repeated with a sinusoidal excitation of $\hat{u}_{\mathrm{ex}} = 250$ V and an offset of $U_{\mathrm{off}} = +250$ V [14]. With a view to avoiding plastic deformations and mechanical damages of the APA, the excitation frequency f was kept below the first resonance. Figure 10.17a and b depict the measured velocity amplitudes $\hat{v}_y(f)$ at the POI for the hinges of type A and type B, respectively. Compared to the measurement results in Fig. 10.16a and b, the achieved velocity amplitudes are much higher. However, they do not coincide with the amplitudes that arise from multiplying the curves in Fig. 10.16 by the factor 250, i.e., 250 V/1 V. This circumstance can be ascribed to the nonlinear behavior of stack actuator and frame. The nonlinearity gets also visible in the total harmonic distortion *THD* relating the energy of the harmonics to the entire energy of a signal [12]. For the small excitation voltage $\hat{u}_{\mathrm{ex}} = 1.5$ V, *THD* is always lower than 5% in the considered frequency range, while it takes values up to 15% at $f = 80$ Hz for $\hat{u}_{\mathrm{ex}} = 250$ V.

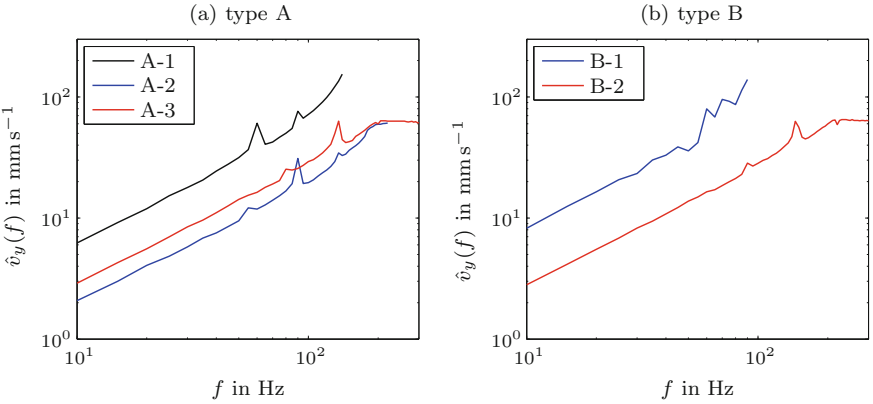

Fig. 10.17 Measured velocity amplitudes $\hat{v}_y(f)$ of APA at POI for hinges of **a** type A and **b** type B; amplitude of excitation voltage $\hat{u}_{ex} = 250\,V$

Summing up, it can be stated that linear FE simulations allow predicting the frequency-dependent behavior of an APA qualitatively. As the simulation and measurement results demonstrated, one can build up a compact APA that exceeds velocity amplitudes of 50 mms^{-1} at an excitation frequency of 80 Hz. The required excitation voltages are in the range of a few hundred volts.

10.3 Piezoelectric Trimorph Actuators

Piezoelectric bending actuators like bimorph and trimorph actuators provide large mechanical deflections in short periods of time. Therefore, they are mostly utilized as mechanical switches in various applications, e.g., in circular knitting machines. However, the large deflections of those actuators might be also interesting for positioning tasks. In this section, let us verify the suitability of a piezoelectric trimorph actuator for such tasks. Section 10.3.1 deals with Preisach hysteresis modeling to describe the hysteretic behavior of the investigated actuator. Since positioning demands the precise knowledge of the electrical actuator excitation, model-based hysteresis compensation is exploited and characterized in Sect. 10.3.2.

10.3.1 Preisach Hysteresis Modeling for Trimorph

In Fig. 10.18, one can see the investigated trimorph actuator 427.0086.12F from the company Johnson Matthey Piezo Products GmbH [9]. This bending actuator containstwo piezoceramic layers (ferroelectric material M1100), both polarized in

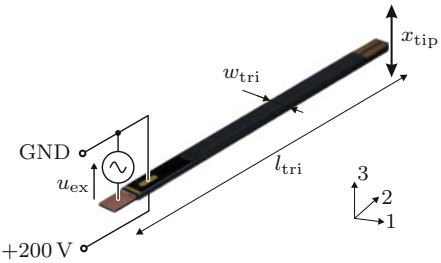

Fig. 10.18 Piezoelectric trimorph actuator 427.0086.12F manufactured by Johnson Matthey Catalysts GmbH; total length l_{tri} and width w_{tri}; electrical excitation u_{ex}; tip deflection x_{tip}

Table 10.7 Specifications of investigated trimorph actuator 427.0086.12F

Thickness h_{layer} of a single piezoceramic layer	260 µm
Thickness h_{int} of the intermediate layer	240 µm
Total thickness h_{tri} of the trimorph actuator	780 µm
Width w_{tri} of the trimorph actuator	2.1 mm
Length l_{tri} of the trimorph actuator	49 mm
Maximum permissible excitation voltage u_{ex}	230 V

positive 3-direction. They are mechanically linked through an additional intermediate layer, which does not exhibit piezoelectric properties and serves as central electrode. The most important specifications of the trimorph actuator are listed in Table 10.7. Due to the chosen electrical connection assignment (see Fig. 10.18), the actuator will deflect in 3-direction if an electrical excitation signal $u_{\mathrm{ex}} \neq 100\,\mathrm{V}$ is applied. Considering linear material behavior, bending in positive 3-direction arises for $u_{\mathrm{ex}} > 100\,\mathrm{V}$, while an excitation signal $u_{\mathrm{ex}} < 100\,\mathrm{V}$ causes bending in negative 3-direction.

Hereinafter, we concentrate on tip deflections x_{tip} for the case that the investigated trimorph actuator is fixed at the other end. Since x_{tip} can reach values up to 1 mm, an optical triangulation position sensor was used for nonreactive displacement measurements [4]. With regard to practical applications of the trimorph actuator in positioning tasks, x_{tip} as function of u_{ex} represents the decisive transfer behavior. To characterize this transfer behavior, a unipolar electrical excitation signal $u_{\mathrm{ex}}(t)$ of sinusoidal shape was utilized which features decreasing amplitudes and a frequency of $f = 0.1\,\mathrm{Hz}$ [34]. The results $x_{\mathrm{tip}}(u_{\mathrm{ex}})$ in Fig. 10.19 clearly indicate that the investigated trimorph actuator shows strongly pronounced hysteresis. Even for small excitation signals, the hysteresis will not be negligible if precise positioning is required. It is for this reason very important to predict x_{tip} with respect to u_{ex}. Again, let us exploit Preisach hysteresis modeling, in particular the generalized Preisach hysteresis operator $\mathcal{H}_{\mathrm{G}}$ (see Sect. 6.6). The model parameters (e.g., B and h_1) were identified by means of adjusting simulations to measured hysteresis curves $x_{\mathrm{tip}}(u_{\mathrm{ex}})$. In doing so, an offset of 100 V has to be added because the trimorph actuator remains in its neutral position (i.e., $x_{\mathrm{tip}} = 0$) for the excitation signal $u_{\mathrm{ex}} = 100\,\mathrm{V}$. As the comparisons of measurements and simulations in Fig. 10.19a and b (magnified detail) demonstrate, Preisach hysteresis modeling allows precise prediction of tip

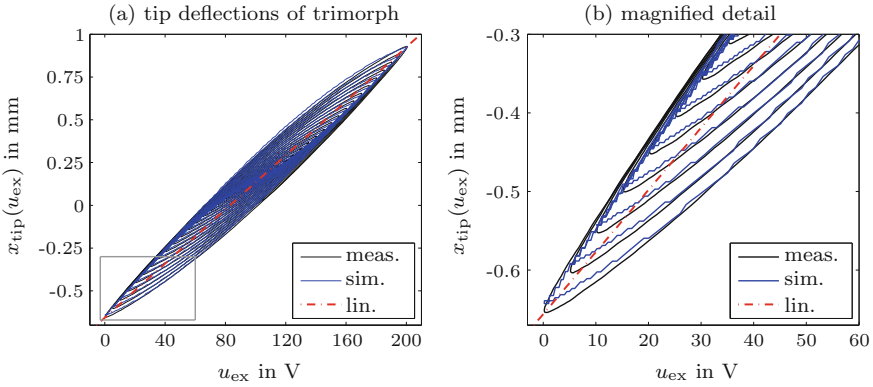

Fig. 10.19 **a** Measured and simulated hysteresis curves $x_{\mathrm{tip}}(u_{\mathrm{ex}})$ as well as linearization; **b** magnified detail of **a**; piezoelectric trimorph actuator 427.0086.12F

deflections. This holds for the entire working area of the investigated trimorph actuator. In contrast, the assumption of linear material behavior, which yields the linearized tip deflection x_{linear}

$$x_{\mathrm{linear}} = x_{\mathrm{meas,min}} + \frac{x_{\mathrm{meas,max}} - x_{\mathrm{meas,min}}}{u_{\mathrm{ex,max}} - u_{\mathrm{ex,min}}} u_{\mathrm{ex}} \tag{10.10}$$

will lead to remarkable deviations between predicted results and measurements. Here, the expressions $x_{\mathrm{meas,min}}$ and $x_{\mathrm{meas,max}}$ stand for minimum and maximum tip deflections that are achieved through the excitation signals $u_{\mathrm{ex,min}}$ and $u_{\mathrm{ex,max}}$ in the considered working area, respectively.

10.3.2 Model-Based Hysteresis Compensation for Trimorph

The previous results have proven that Preisach hysteresis modeling is well suited to predict the hysteretic behavior of the investigated piezoelectric trimorph actuator. However, positioning tasks in practical applications demand knowledge of the electrical excitation signal u_{ex} to achieve the desired actuator's tip deflection x_{tar}. One has, therefore, to invert the generalized Preisach hysteresis operator leading to $\mathcal{H}_{\mathrm{G}}^{-1}$. For this purpose, let us apply the same inversion procedure as in Sect. 6.8. Figure 10.20a illustrates the general approach of the underlying model-based hysteresis compensation: Starting from the desired target output $x_{\mathrm{tar}}(t)$ with respect to time t, we determine the electrical excitation signal $u_{\mathrm{inv}}(t)$ through $\mathcal{H}_{\mathrm{G}}^{-1}$. The resulting tip deflections $x_{\mathrm{model}}(t)$ of the trimorph actuator are then measured and compared to $x_{\mathrm{tar}}(t)$. Besides, the investigated actuator was excited with the electrical signal $u_{\mathrm{linear}}(t)$, which results from inverting (10.10) and represents the case that the

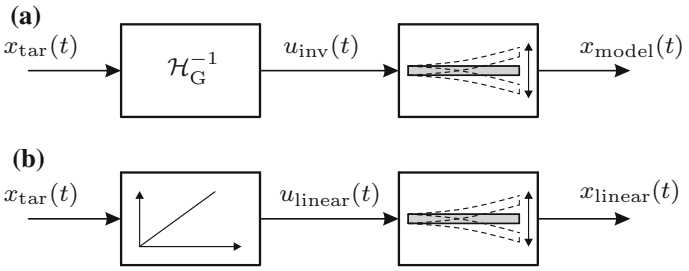

Fig. 10.20 Block diagram to achieve desired mechanical deflections $x_{\mathrm{tar}}(t)$ of the trimorph actuator for **a** model-based hysteresis compensation and **b** uncompensated case (i.e., linearization); determined quantities: $u_{\mathrm{inv}}(t)$ and $u_{\mathrm{linear}}(t)$; measured quantities: $x_{\mathrm{model}}(t)$ and $x_{\mathrm{linear}}(t)$

hysteretic behavior of the actuator is not taken into account (see Fig. 10.20b). For this excitation, the acquired tip deflections $x_{\mathrm{linear}}(t)$ are also compared to $x_{\mathrm{tar}}(t)$.

As already mentioned in Sect. 10.3.1, the parameters of the generalized Preisach hysteresis operator were identified on basis of sinusoidal excitations signal featuring decreasing amplitudes. With a view to evaluating the performance of the model-based hysteresis compensation for the piezoelectric trimorph actuator, a target quantity $x_{\mathrm{tar}}(t)$ should be chosen that remarkably differs from the one considered during parameter identification. Figures 10.21b and 10.22b display such target quantities containing several local minima and maxima as well as different slopes of the tip deflection with respect to time. The top panels (Figs. 10.21a and 10.22a) depict the applied excitation signals $u_{\mathrm{inv}}(t)$ and $u_{\mathrm{linear}}(t)$ of the investigated trimorph actuator resulting from model-based hysteresis compensation and linearization (see Fig. 10.20), respectively. Although the chosen target quantities are of completely other shape as the identification signal, $\mathcal{H}_{\mathrm{G}}^{-1}$ yields normalized relative deviations $|\epsilon_{\mathrm{r}}|$ (magnitude) between $x_{\mathrm{model}}(t)$ and $x_{\mathrm{tar}}(t)$ that always stay below 5%. In contrast, the normalized relative deviations for the linearization approach partially exceed 15%, which confirms the relevance of model-based hysteresis compensation for the trimorph actuator in positioning tasks. Nevertheless, especially steep changes in $x_{\mathrm{tar}}(t)$ followed by a constant value are accompanied by large relative deviations ϵ_{r}. This fact can be ascribed to the creep behavior of the actuator that is not taken into account even if we conduct generalized Preisach hysteresis modeling [34].

In various practical applications, positioning actuators have to move exclusively between two positions at constant speed. For the piezoelectric trimorph actuator, it is, thus, desired that the slope $\partial x_{\mathrm{tar}}(t)\,/\partial t$ (i.e., velocity) of the tip deflections remains constant between the two positions. Consequently, the target tip deflection $x_{\mathrm{tar}}(t)$ of the actuator with respect to time corresponds to a triangular waveform. Figure 10.23a shows such a tip deflection oscillating between the positions ± 0.580 mm with the frequency $f = 0.1$ Hz. To obtain the desired tip deflections $x_{\mathrm{tar}}(t)$ of the investigated trimorph actuator, we have to consider its hysteric behavior through model-based hysteresis compensation (see Fig. 10.20a). By means of the inverted generalized Preisach hysteresis operator $\mathcal{H}_{\mathrm{G}}^{-1}$, the measured tip deflections $x_{\mathrm{model}}(t)$ oscillate

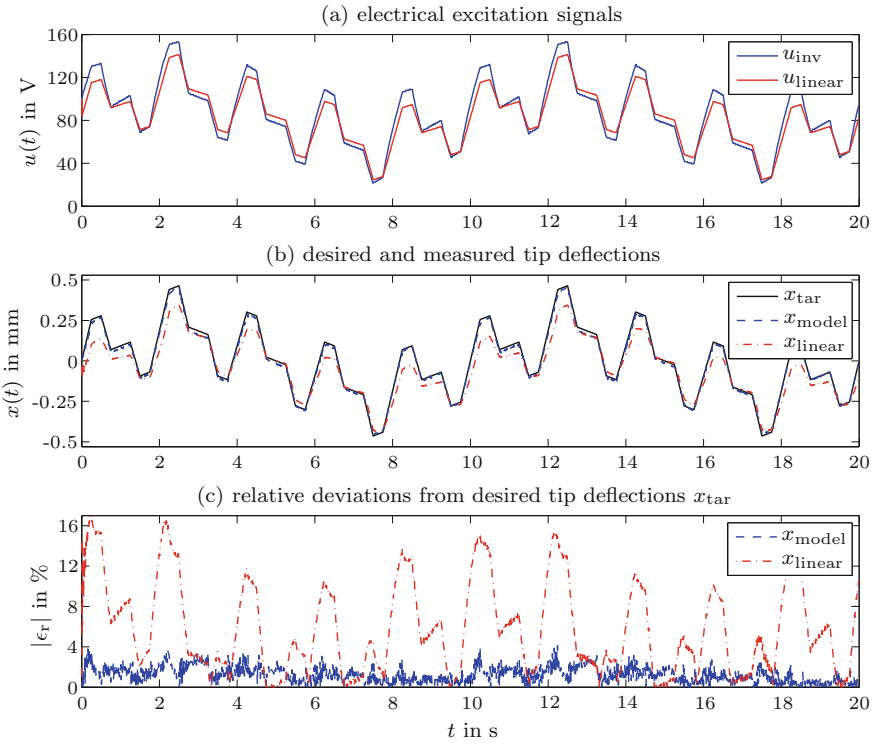

Fig. 10.21 **a** Electrical excitation signals $u_{\text{inv}}(t)$ and $u_{\text{linear}}(t)$ for model-based hysteresis compensation and uncompensated case, respectively; **b** desired tip deflections $x_{\text{tar}}(t)$ and measured ones $x_{\text{model}}(t)$ as well as $x_{\text{linear}}(t)$; **c** normalized relative deviations $|\epsilon_{\text{r}}|$ in % (magnitude); piezoelectric trimorph actuator 427.0086.12F

between $+0.584$ mm and -0.573 mm. The normalized relative deviations $|\epsilon_{\text{r}}|$ (magnitude) in Fig. 10.23b reveal that $x_{\text{model}}(t)$ and $x_{\text{tar}}(t)$ do not only coincide well for maximum as well as minimum tip deflections but also in between [34, 35]. On the other hand, when we neglect the hysteretic behavior of the trimorph actuator meaning linearization according to Fig. 10.20b, the resulting tip deflections $x_{\text{linear}}(t)$ will remarkably differ from $x_{\text{tar}}(t)$. For instance, $x_{\text{linear}}(t)$ oscillates between $+0.476$ mm and -0.565 mm. While the maximum of $|\epsilon_{\text{r}}|$ for model-based compensation is less than 3%, assuming linear behavior can lead to values greater than 12%.

Actually, the tip deflections x_{tip} of the investigated trimorph actuator exhibit a certain frequency dependence. If resonance phenomena are not considered, an increasing frequency f of the electrical excitation signal u_{ex} will reduce the achievable tip deflection. Figure 10.23c illustrates this behavior with the aid of hysteresis curves $x_{\text{tip}}(u_{\text{ex}}, f)$, which result from sinusoidal excitation signals featuring different frequencies. For the excitation voltage $u_{\text{ex}} = 200$ V, the maximum tip deflection decreases from 1.003 mm for 0.01 Hz to 0.842 mm for 10 Hz. As a matter of course,

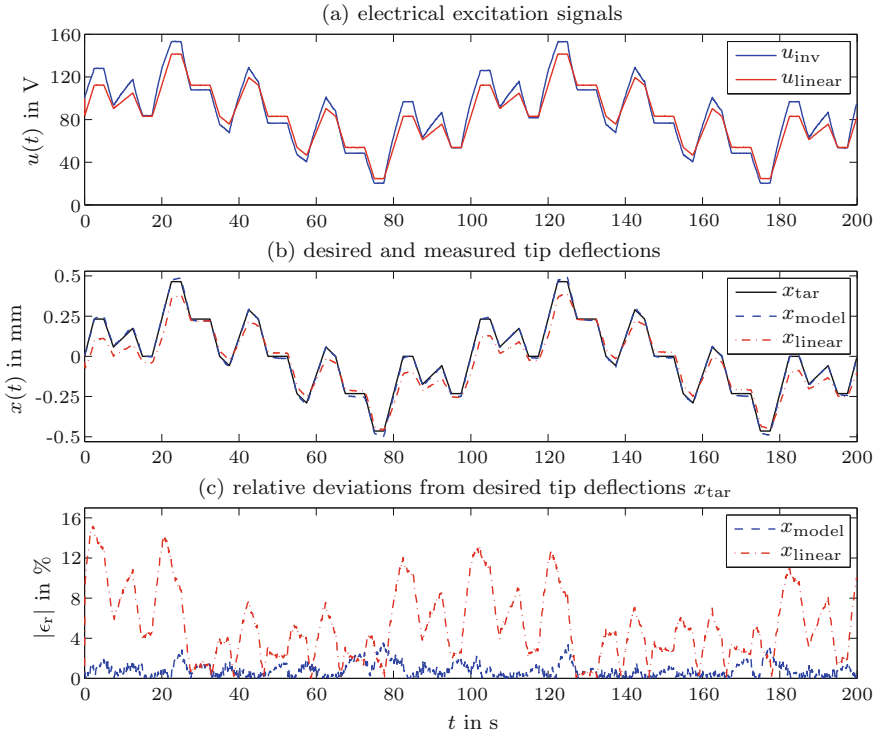

Fig. 10.22 **a** Electrical excitation signals $u_{\text{inv}}(t)$ and $u_{\text{linear}}(t)$ for model-based hysteresis compensation and uncompensated case, respectively; **b** desired tip deflections $x_{\text{tar}}(t)$ and measured ones $x_{\text{model}}(t)$ as well as $x_{\text{linear}}(t)$; **c** normalized relative deviations $|\epsilon_{\text{r}}|$ in % (magnitude); piezoelectric trimorph actuator 427.0086.12F

we have to consider the frequency-dependent behavior in Preisach hysteresis modeling for the trimorph actuator. Similar to Sect. 6.6.4, the excitation frequency can be incorporated in modeling through varying only a few parameters. Here, it is sufficient to exclusively alter the model parameter h_2 with respect to f [34]. Figure 10.23d depicts the identified values for $h_2(f)$ that can serve as data points for the smoothing function (cf. (6.29, p. 233))

$$\psi_{\text{smooth}}(f) = \varsigma_1 + \varsigma_2 \cdot f^{\varsigma_3} \tag{10.11}$$

with the function parameters ς_i. On basis of this smoothing function, the generalized Preisach hysteresis operator was inverted, which is required for model-based hysteresis compensation of actuator deflections. Figure 10.23e contains the target tipdeflection $x_{\text{tar}}(t)$ of triangular shape with a frequency of 10 Hz as well as the

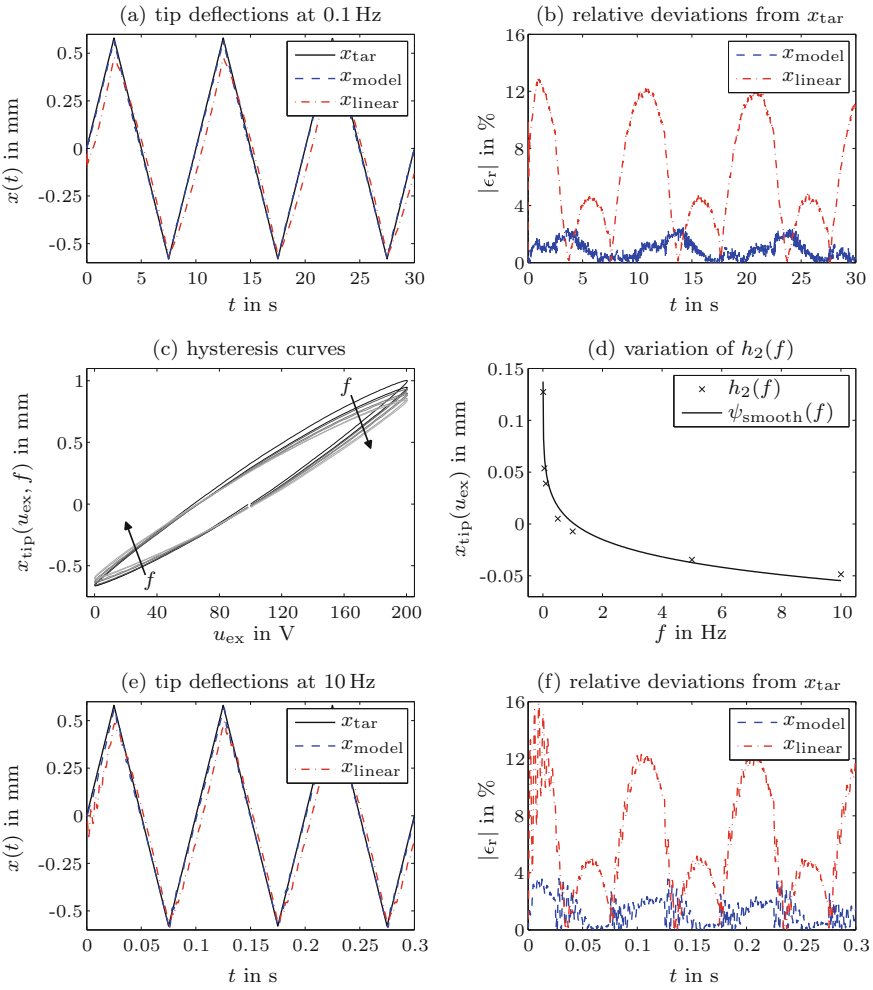

Fig. 10.23 **a** Desired tip deflections $x_{\mathrm{tar}}(t)$ (triangular; frequency $f = 0.1\,\mathrm{Hz}$) and measured ones $x_{\mathrm{model}}(t)$ as well as $x_{\mathrm{linear}}(t)$; **b** normalized relative deviations $|\epsilon_{\mathrm{r}}|$ in % (magnitude); **c** measured hysteresis curves $x_{\mathrm{tip}}(u_{\mathrm{ex}}, f)$ with respect to excitation frequency f; **d** variation of model parameter $h_2(f)$ as well as smoothing function $\psi_{\mathrm{smooth}}(f)$ according to (10.11) with the parameters $\varsigma_1 = 0.5042$, $\varsigma_2 = -0.5030$, and $\varsigma_3 = 0.0457$; **e** desired tip deflections $x_{\mathrm{tar}}(t)$ (triangular; frequency $f = 10\,\mathrm{Hz}$) and measured ones $x_{\mathrm{model}}(t)$ as well as $x_{\mathrm{linear}}(t)$; **f** normalized relative deviations $|\epsilon_{\mathrm{r}}|$ in % (magnitude); piezoelectric trimorph actuator 427.0086.12F

measured quantities $x_{\mathrm{model}}(t)$ and $x_{\mathrm{linear}}(t)$. Due to the steep changes of the electrical excitation, there occur high-frequency mechanical vibrations of the actuator tip that are not covered by phenomenological Preisach hysteresis modeling. However, once again, the model-based hysteresis compensation provides much more reliable tip deflections of the investigated trimorph actuator than the linearization (see Fig. 10.23f).

10.4 Piezoelectric Motors

A piezoelectric motor is a device that converts electrical energy into mechanical energy. In doing so, piezoelectric motors perform either translational or rotational motions. Depending on the movement type, they are designated as *linear piezoelectric motors* or *rotary piezoelectric motors*. Figure 10.24 depicts the principle components of piezoelectric motors. The components can be grouped into the vibrator and the slider [27]. While the vibrator is composed of a piezoelectric driving element and an elastic vibrator piece, the slider contains a friction coating as well as an elastic sliding piece. The motion of vibrator and slider against each other leads to the mechanical output of the piezoelectric motor. Since the arising component movements are often in the ultrasonic range, piezoelectric motors are also termed piezoelectric ultrasonic motors [37].

In contrast to electromagnetic motors, one can easily build up efficient piezoelectric motors with sizes smaller than $1\,\mathrm{cm}^{-3}$. This stems from the fact that the conversion of electrical into mechanical energy does not depend on the size of piezoelectric motors. The conversion efficiency is predominantly determined by the utilized piezoelectric material and the basic motor design. As a result, we can achieve a large ratio of mechanical power to motor weight. In general, linear and rotary piezoelectric motors provide low translation velocities and slow rotational speeds, respectively [23, 27, 28]. Further advantages of piezoelectric motors over electromagnetic motors lie in the simple structure, easy production process, high retention forces, and negligible impacts of external magnetic fields on the motor performance. However, piezoelectric motors demand a high-frequency power supply and mostly offer less durability due to friction wear. Besides, the ratio of available force to generated velocity decreases with increasing velocities of linear piezoelectric motors. The same holds for the ratio of available torque to generated rotational speed for increasing rotational speeds of rotary piezoelectric motors. Nevertheless, since the advantages of piezoelectric motors often outweigh their disadvantages, they are used in various applications, e.g., as space-saving and efficient drives in camera lenses [1, 18].

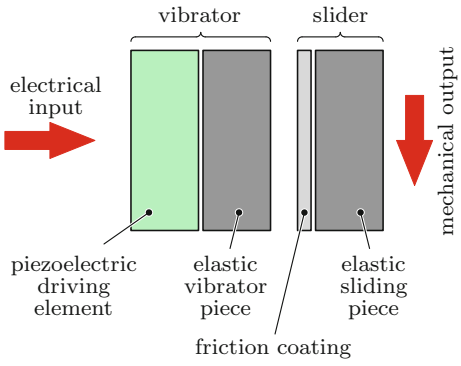

Fig. 10.24 Principle components of piezoelectric motors that convert electrical inputs into mechanical outputs

It is not surprising that the piezoelectric elements strongly influence the performance of piezoelectric motors. Due to this fact, piezoelectric motors are mostly based on piezoceramic materials because such materials offer high electromechanical coupling factors (see Sect. 3.6). To avoid excessive heat development during operation, especially in case of motors that exploit the resonance mode, one should use ferroelectrically hard PZT materials. Heat-induced depolarization can be prevented if the piezoceramic material additionally exhibits a high Curie temperature ϑ_C.

There can be found many different designs of piezoelectric motors in the literature. In the following, we will briefly discuss selected examples of linear piezoelectric motors (see Sect. 10.4.1) and rotary piezoelectric motors (see Sect. 10.4.2).

10.4.1 Linear Piezoelectric Motors

The selected examples of linear piezoelectric motors include inchworm, stepper as well as slip-stick motors.

Inchworm Motors

Inchworm motors can be considered as one the oldest categories of piezoelectric motors [3]. The name is justified by the underlying motion sequence, which is reminiscent of the movement of an inchworm. Basically, an inchworm motor contains two clamp actuators, a feed actuator, and two end plates and a slider (see Fig. 10.25) [5]. Because of the required strokes, longitudinal PSAs usually serve as clamp and feed actuators. A single motion sequence of an inchworm motor comprises six steps (see Fig. 10.26).

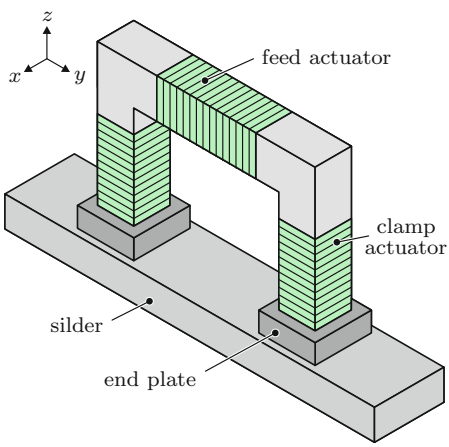

Fig. 10.25 Principle setup of piezoelectric inchworm motor; slider can be moved in positive and negative y-direction

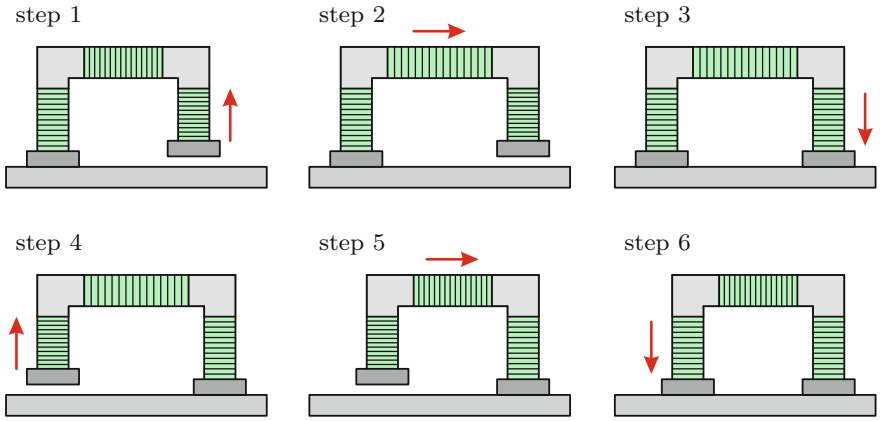

Fig. 10.26 Single motion sequence of inchworm motor; red arrows indicate direction of current actuator expansion and contraction

- Step 1: Releasing the right clamping by contraction of the right clamp actuator.
- Step 2: Forward motion by expansion of the feed actuator.
- Step 3: Expansion of the right clamp actuator, i.e., activation of the right clamping.
- Step 4: Releasing the left clamping by contraction of the left clamp actuator.
- Step 5: Contraction of the feed actuator.
- Step 6: Expansion of the left clamp actuator, i.e., activation of the left clamping.

After step 6, the motion sequence starts again with step 1. If the center of the feed actuator is fixed in space, the slider will move from the right to the left. By exchanging right through left and left through right in the motion sequence, the slider will move from the left to the right.

In general, inchworm motors offer high positioning accuracy, high rigidity, and a travel distance, which is infinite from the theoretical point of view. Even though the deployed PSAs provide high velocities, the complicated motion sequence results in greatly reduced travel speeds. The friction-type connection between end plates and slider in conventional inchworm motors leads, furthermore, to limited feed and holding forces. That is the reason why many efforts have been recently made to replace the friction-type connection by a positive-locking connection, which can be realized by equipping both the end plates and the slider with an appropriate interlocking [2, 19]. As a matter of fact, the lateral distance between adjacent teeth determines the minimal travel distance. From there, it makes sense to use a tight interlocking. If the end plates and the slider are made of silicon, one is able to fabricate the interlocking by anisotropic etching. A more robust interlocking can be obtained by using components that are made of hardened steel. In this case, the fabrication of a tight interlocking calls for laser ablation methods.

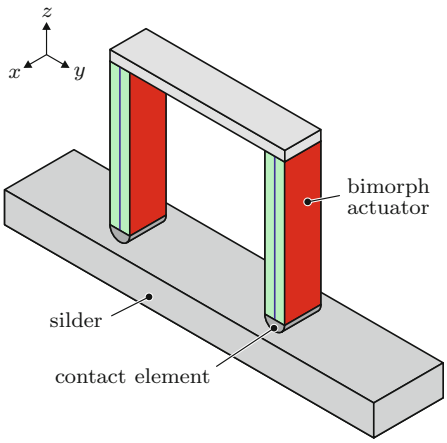

Fig. 10.27 Principle setup of piezoelectric stepper motor; slider can be moved in positive and negative y-direction

Stepper Motors

The working principle of piezoelectric stepper motors is quite similar to that of inchworm motors. The main difference between both motor types lies in the feed actuator, which is not required for piezoelectric stepper motors [16, 26]. Stepper motors are commonly based on either piezoelectric bimorph actuators or combinations of longitudinal and shear PSAs. Here, let us describe the working principle for piezoelectric bimorph actuators. Figure 10.27 displays a fundamental setup, which consists of two piezoelectric serial bimorph actuators with contact elements and a slider that gets mechanically pressed against at least one actuator. Both piezoelectric bimorph actuators are connected at their top end to the housing. The two piezoelectric bars inside a single bimorph actuator are polarized in opposite direction and have to be controlled separately. In Fig. 10.28, one can see a single motion sequence of a piezoelectric serial bimorph actuator as well as the sinusoidal excitation voltages $u_{\mathrm{ex;A}}(t)$ and $u_{\mathrm{ex;B}}(t)$ of both piezoelectric bars. It is possible to distinguish between three excitation scenarios.

- $u_{\mathrm{ex;A}}(t) = u_{\mathrm{ex;B}}(t)$: The bimorph actuator keeps its shape. If both voltages are negative, the bimorph actuator will expand (state I in Fig. 10.28a). If both voltages are positive, the bimorph actuator will contract (state III in Fig. 10.28a).
- $u_{\mathrm{ex;A}}(t) > u_{\mathrm{ex;B}}(t)$: The bimorph actuator bends to the right because the left bar expands and the right bar contracts (state II in Fig. 10.28a).
- $u_{\mathrm{ex;A}}(t) < u_{\mathrm{ex;B}}(t)$: The bimorph actuator bends to the left because the left bar contracts and the right bar expands (state IV in Fig. 10.28a).

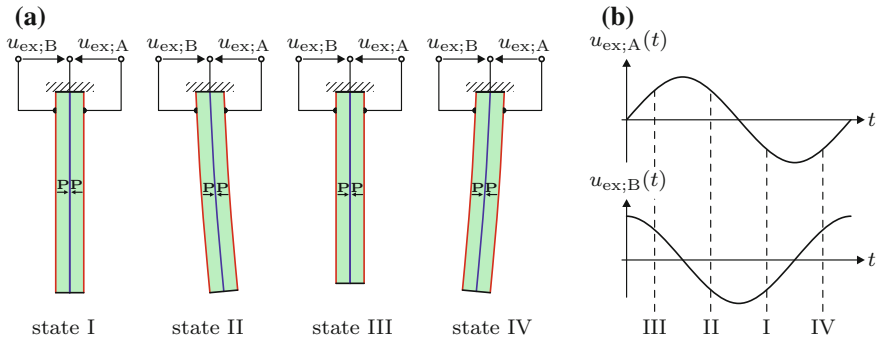

Fig. 10.28 **a** Motion sequence of single piezoelectric serial bimorph actuator; direction of electric polarization **P**; **b** electrical excitation signals $u_{ex;A}(t)$ and $u_{ex;B}(t)$ for elliptical motion of bimorph tip

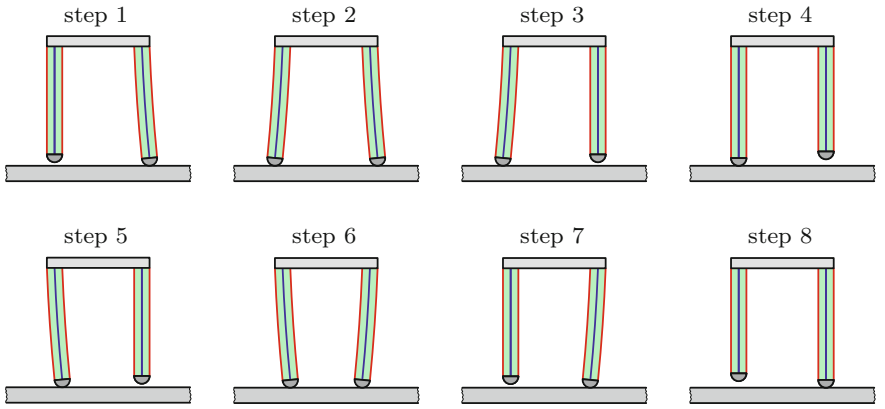

Fig. 10.29 Single motion sequence of piezoelectric stepper motor; slider moves from left to right

When $u_{ex;A}(t)$ and $u_{ex;B}(t)$ have identical amplitude and frequency but exhibit a phase difference of 90°, the lower end of the piezoelectric bimorph actuator performs an elliptical motion. By exciting both bimorph actuators (i.e., the four piezoelectric bars) appropriately, the slider of the piezoelectric stepper motor moves due to this elliptical motion. Figure 10.29 shows the motion sequence comprising eight steps for a slider movement from the left to the right. If the piezoelectric bimorph actuators are regarded as legs, the resulting motion sequence will reminiscent of a walking human.

Slip-Stick Motors

Piezoelectric slip-stick motors exploit the inertial principle, i.e., the inertia of moving objects [7, 36]. In Fig. 10.30a, one can see a possible setup and the underlying working principle of such a motor. The setup contains a longitudinal PSA, a drive shaft, and a moving part. While the left-hand side of the PSA is fixed, its right-hand

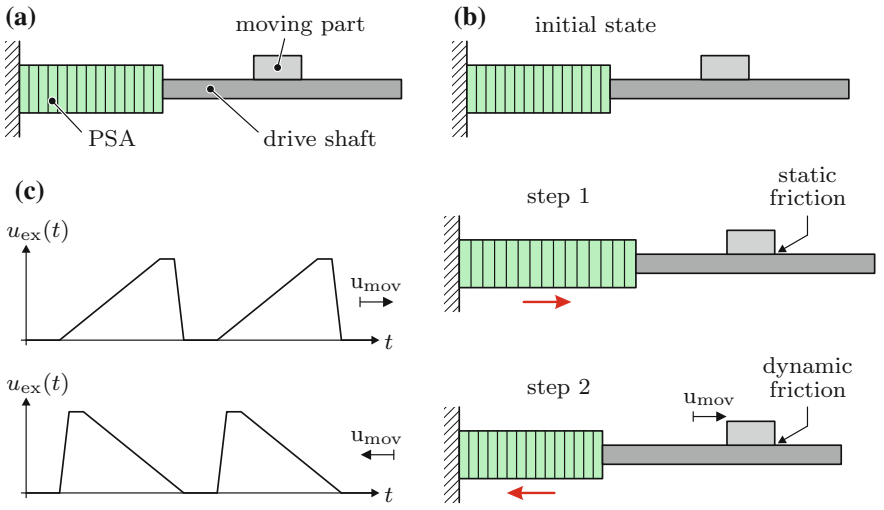

Fig. 10.30 **a** Possible setup of piezoelectric slip-stick motor; **b** initial state and steps of single motion sequence; displacement u_{mov} of moving part; red arrow indicates expansion and contraction of longitudinal PSA; **c** electrical excitation voltage $u_{ex}(t)$ of PSA for shifts of moving part to right and left, respectively

side is attached to the drive shaft. The moving part, which represents the slider of the piezoelectric motor, is located on the drive shaft. A single motion sequence of the considered slip-stick motor comprises two steps.

- Step 1: Slow expansion of the PSA.
- Step 2: Fast contraction of the PSA.

The steps can be achieved by exciting the PSA with the electrical voltages $u_{ex}(t)$ as shown at the top of Fig. 10.30c. During step 1, the static friction between moving part and drive shaft leads to a slow shift of both components (see Fig. 10.30b). Due to the fast PSA contraction during step 2, the static friction between moving part and drive shaft converts into dynamic friction. This stems from the fact that the inertia force acting on the moving part exceeds the static friction force. As a result, the moving part alters its position by u_{mov}. In the present case, the moving part is shifted to the right. If the speed of PSA expansion and contraction is exchanged (i.e., fast expansion and slow contraction), which results from $u_{ex}(t)$ at the bottom of Fig. 10.30c, the moving part will be shifted to the left. The attainable velocity of the moving part mainly depends on the duration of the slow PSA deformation. When this duration is too short, the accelerations will yield high inertia forces exceeding the static friction force between moving part and drive shaft. Consequently, the moving part will remain at the same position.

10.4.2 Rotary Piezoelectric Motors

The selected examples of rotary piezoelectric motors include standing wave, traveling wave as well as so-called Kappel motors.

Standing Wave Motors

As the name already suggests, standing wave motors are based on the formation of standing waves. Before we discuss rotary piezoelectric motors that exploit standing waves, let us regard a one-dimensional standing wave from the mathematical point of view. Such a wave can be expressed as

$$u_S(x,t) = \hat{u}_S \cos(kx)\cos(\omega t) \tag{10.12}$$

with the displacement amplitude $\hat{u}_S$, the wave number k, the position x, the angular frequency ω, and the time t, respectively. The resulting displacement $u_S(x,t)$ exhibits fixed nodes at which $u_S(x,t) = 0$ holds as well as fixed antinodes at which $u_S(x,t) = \hat{u}_S$ holds.

In the context of rotary piezoelectric motors, one makes use of shifts of vibrator against slider due to standing waves [23, 27]. Figure 10.31a depicts a simple setup of a rotary standing wave motor. It comprises a longitudinal PSA that is spatially fixed at one end, a plunger being connected to the other end of the PSA, and a rotor. According to the definition in Fig. 10.24, the combination of PSA and plunger represents the vibrator, while the rotor is the slider. To generate rotational movements of the rotor, we need a slight angle Θ_M between the central axis of the plunger and the surface normal of the rotor surface, where the plunger is pressed to the rotor. If the PSA expands, the arising contact area will move along the rotor surface. In case of a sufficient static friction between plunger and rotor, this plunger movement yields a rotational movement of the rotor. Not surprisingly, large rotational movements can be reached when the longitudinal PSA excites a standing wave that offers antinodes at the plunger tip.

The superposition of the longitudinal PSA stroke and the movement along the rotor surface results in an almost elliptical motion of the plunger tip with respect to a fixed coordinate system. Figure 10.31b illustrates a possible tip motion with the characteristic points A and B. From A to B, the plunger tip contacts the rotor. That is the reason why the tip motion corresponds to the rotor surface. Since there does not exist any contact from B to A, plunger and rotor do not affect each other. The plunger tip undergoes, thus, an elliptical motion. Although the tip does not contact the rotor from B to A, the rotor continues rotating, which is a consequence of the nonzero rotor's moment of inertia I_R. A small value of I_R is accompanied by strong fluctuations of the rotor movement. Of course, the driven load also influences I_R and, therefore, the uniformity of the rotor movement.

By using only one vibrator (i.e., one longitudinal PSA with plunger) as shown in Fig. 10.31a, we are restricted to a single direction of rotation. When the piezoelectric motor contains a second vibrator, which is appropriately arranged, it is possible to introduce rotational movements in the other direction of rotation. For the

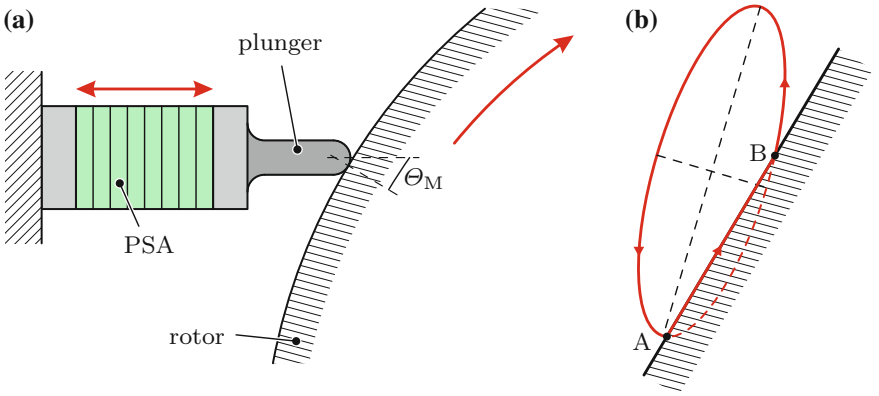

Fig. 10.31 **a** Simple setup of rotary piezoelectric standing wave motor with single longitudinal PSA; red arrows indicate direction of movements; **b** magnified plunger's tip motion at contact area with characteristic points A and B [27]

given example, this can be achieved by placing the second vibrator on the opposite side of the rotor. There also exist rotary piezoelectric motors, which are based on a butterfly-shaped vibrator that contains both vibrators [37]. In further motor designs, the piezoelectric vibrators directly act on the front surface of the rotor.

Traveling Wave Motors

Just as in case of standing wave motors, let us start with a one-dimensional traveling wave from the mathematical point of view. The location-dependent as well as time-dependent displacement $u_T(x, t)$ of such a wave can be expressed as

$$u_T(x, t) = \hat{u}_T \cos(kx - \omega t) \tag{10.13}$$

with the displacement amplitude $\hat{u}_T$. In contrast to a standing wave, a traveling wave contains neither fixed nodes nor fixed antinodes. However, by using basic trigonometric relations, we are able to convert (10.13) into

$$\begin{aligned} u_T(x, t) &= \hat{u}_T \cos(kx) \cos(\omega t) + \hat{u}_T \cos\left(kx - \frac{\pi}{2}\right) \cos\left(\omega t - \frac{\pi}{2}\right) \\ &= \hat{u}_T \cos(kx) \cos(\omega t) + \hat{u}_T \sin(kx) \sin(\omega t) \ . \end{aligned} \tag{10.14}$$

Both terms of the sum represent standing waves, whose phases differ by $\pi/2$ from each other in space and time. Thus, a traveling wave can be generated by superimposing two standing waves. Note that this is not limited to the fundamental wave but also holds for the nth harmonic $u_{T;n}(x, t)$ of a traveling wave, which is given by

$$u_{T;n}(x, t) = \hat{u}_{T;n} \cos(nkx - \omega t) \ . \tag{10.15}$$

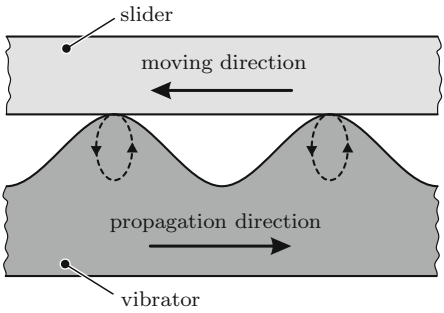

Fig. 10.32 Principle of piezoelectric traveling wave motors; slider movement is opposite to propagation direction of surface wave

The decomposition into two standing waves becomes then

$$u_{T;n}(x,t) = \hat{u}_{T;n}\cos(nkx)\cos(\omega t) + \hat{u}_{T;n}\sin(nkx)\sin(\omega t) \ . \tag{10.16}$$

From there, it should be possible to build up a piezoelectric motor that exploits traveling waves by means of two standing waves. This fact is decisive because we can easily generate standing waves inside a structure of finite size through piezoelectric actuators.

Figure 10.32 shows the underlying principle of common piezoelectric traveling wave motors. Let us assume an elastic wave, which propagates from the left to the right on the vibrator surface that faces the slider. Such traveling wave corresponds to a surface wave (Rayleigh wave) and, therefore, comprises longitudinal as well as transverse waves. A surface particle of the vibrator undergoes an elliptical motion in counterclockwise direction. The contact areas between vibrator and slider arise at the positive local maxima of the propagating surface wave. When the static friction between vibrator and slider at these areas is sufficient, the longitudinal part of the elliptical motion will lead to a slider movement against the direction, in which the surface wave propagates. Not surprisingly, the contact mechanism is decisive for the operational characteristic (e.g., rotational speed) of traveling wave motors [29].

In Fig. 10.33a, one can see a well-known practical implementation of a rotary piezoelectric motor that is based on traveling waves. This so-called *Sashida motor* consists of a piezoceramic ring, an elastic ring, a slider, and a rotor [23, 27]. While the elastic ring is linked to the piezoelectric ring, the slider is linked to the rotor. The piezoceramic ring contains 16 active areas, which are polarized in either positive or negative thickness direction (see Fig. 10.33b). The active areas are grouped into the two parts A and B, each with eight elements being contacted by common electrodes. In peripheral direction, the active areas feature the geometric dimension $\lambda_T/2$, whereby λ_T stands for the wavelength of the resulting surface wave on the piezoceramic ring. The spacings (i.e., areas without electrodes) between the two parts amount $3/4\lambda_T$ and $\lambda_T/4$, respectively. With the aid of a single part, we can generate a standing wave along the piezoelectric and elastic ring. Relating to the ring's circumference, this standing wave corresponds to the ninth harmonic. The spacings of the part A and B lead to the spatial phase shift $90°/9 = 10°$ of both standing

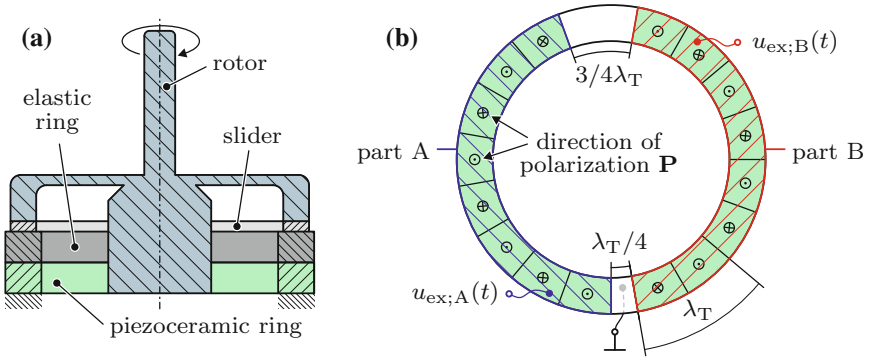

Fig. 10.33 **a** Cross-sectional view of Sashida motor; **b** top view of piezoceramic ring containing 16 active areas with different directions of electric polarization **P** [23, 27]; wavelength λ_T of traveling wave along ring; electrical excitation $u_{ex;A}(t)$ and $u_{ex;B}(t)$ of part A and B, respectively

waves. According to (10.16), it will, thus, be possible to generate a traveling wave along the rings if one part is electrically excited by $\hat{u}_{ex} \sin(\omega t)$ and the other part by $\hat{u}_{ex} \cos(\omega t)$. Exchanging the excitation signals of the parts results in a change of the direction of rotation, e.g., from clockwise to counterclockwise. In each case, the traveling wave yields a rotation of the rotor.

Sashida-type motors are energy-saving as well as thin and do not require gears. On those ground, such piezoelectric rotary motor is often used in camera lenses for autofocusing. There also exist extended versions of Sashida-type motor, which are equipped with a tooth-shaped vibrator to improve the rotation speed of the rotor [37].

Kappel Motors

This special type of rotary piezoelectric motor was invented by KAPPEL in 1999. Similar to piezoelectric standing wave motors, Kappel motors exploit the conversion of linear motions into rotary motions [10, 30]. Figure 10.34 depicts the principle setup of a Kappel motor that consists of two longitudinal PSAs with plungers, a drive ring, and a pivoted rotor with a slightly smaller diameter than the inner diameter of the drive ring. The two PSAs are arranged at 90° to each other and, thus, can move the drive ring in the xy-plane. If this movement takes place along an appropriate circular path, the rotor will roll on the inner surface of the drive ring. Consequently, the rotor undergoes a rotary motion. The circular movement of the drive ring requires electrical PSA excitations with identical amplitudes $\hat{u}_{ex}$ but a phase shift of 90°; i.e., when one PSA is excited by $\hat{u}_{ex} \cos(\omega t)$, the other PSA has to be excited by $\hat{u}_{ex} \sin(\omega t)$. Exchanging the PSA excitations yields the opposite direction of rotation.

With a view to achieving rotary motions in case of smooth surfaces of drive ring and rotor, the static friction between them has to be sufficient. High load torquesmay

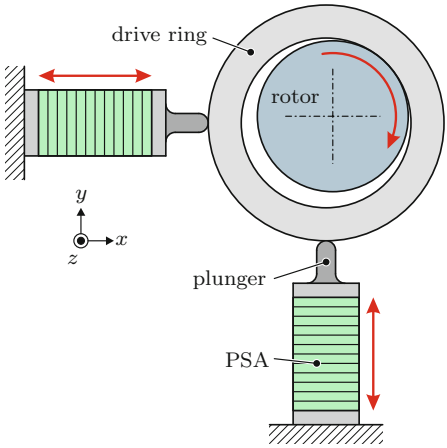

Fig. 10.34 Principle setup of Kappel motor with two longitudinal PSAs; red arrows indicate direction of movements

lead, however, to a malfunction of the motor. That is the reason why several practical implementations of Kappel motors are equipped with a tight interlocking, just as inchworm motors [10]. In doing so, the friction-type connection between drive ring and rotor becomes replaced by a positive-locking connection.

Kappel motors allow a high positioning accuracy, a speed-independent high torque, an outstanding dynamic behavior, and sensorless measurements of load torques. In contrast to many other rotary piezoelectric motors, Kappel motors can be used in a wide speed range. On these grounds, there exist various practical applications for such motors, e.g., electric window lifter. The high production costs compared to conventional electromagnetic motors hamper, nevertheless, the commercial breakthrough of Kappel motors up to now.

References

1. Canon, Inc.: Manufacturer of digital cameras and camcorders (2018). http://www.canon.com/icpd/
2. Chen, Q., Yao, D.J., Kim, C.J., Carman, G.P.: Mesoscale actuator device: micro interlocking mechanism to transfer macro load. Sens. Actuators A Phys. **73**(1–2), 30–36 (1999)
3. Galante, T., Frank, J., Bernard, J., Chen, W., Lesieutre, G.A., Koopmann, G.H.: Design, modeling, and performance of a high force piezoelectric inchworm motor. J. Intell. Mater. Syst. Struct. **10**(12), 962–972 (1999)
4. Göpel, W., Hesse, J., Zemel, J.N.: Sensors Volume 6 - Optical Sensors. VCH, Weinheim (1992)
5. Hegewald, T.: Modellierung des nichtlinearen Verhaltens piezokeramischer Aktoren. Ph.D. thesis, Friedrich-Alexander-University Erlangen-Nuremberg (2007)
6. Heywang, W., Lubitz, K., Wersing, W.: Piezoelectricity: Evolution and Future of a Technology. Springer, Berlin (2008)
7. Hunstig, M.: Piezoelectric inertia motors - a critical review of history, concepts, design, applications, and perspectives. Actuators **6**(1) (2017)
8. Janocha, H.: Actuators - Basics and Applications. Springer, Berlin (2004)

9. Johnson Matthey Piezo Products GmbH: Product portfolio (2018). www.piezoproducts.com
10. Kappel, A., Gottlieb, B., Wallenhauer, C.: Piezoelectric actuator drive (PAD). At-Automatisierungstechnik **56**(3), 128–135 (2008)
11. Kim, J.H., Kim, S.H., Kwaka, Y.K.: Development of a piezoelectric actuator using a three-dimensional bridge-type hinge mechanism. Rev. Sci. Instr. **74**(5), 2918–2924 (2003)
12. Lerch, R.: Elektrische Messtechnik, 7th edn. Springer, Berlin (2016)
13. Lobontiu, N.: Compliant Mechanisms: Design of Flexure Hinges. CRC Press, Boca Raton (2002)
14. Löffler, M., Weiß, M., Wiesgickl, T., Rupitsch, S.J.: Study on analytical and numerical models for application-specific dimensioning of a amplified piezo actuator. Tech. Messen **84**(11), 706–718 (2017)
15. Ma, H.W., Yao, S.M., Wang, L.Q., Zhong, Z.: Analysis of the displacement amplification ratio of bridge-type flexure hinge. Sens. Actuators A Phys. **132**(2), 730–736 (2006)
16. Merry, R.J.E., de Kleijn, N.C.T., van de Molengraft, M.J.G., Steinbuch, M.: Using a walking piezo actuator to drive and control a high-precision stage. IEEE/ASME Trans. Mech. **14**(1), 21–31 (2009)
17. Muraoka, M., Sanada, S.: Displacement amplifier for piezoelectric actuator based on honeycomb link mechanism. Sens. Actuators A Phys. **157**(1), 84–90 (2010)
18. Nikon, Inc.: Manufacturer of digital cameras (2018). http://www.nikon.com/index.htm
19. Park, J., Carman, G.P., Thomas Hahn, H.: Design and testing of a mesoscale piezoelectric inchworm actuator with microridges. J. Intell. Mater. Syst. Struct. **11**(9), 671–684 (2001)
20. PI Ceramic GmbH: Product portfolio (2018). https://www.piceramic.com
21. Polytec GmbH: Product portfolio (2018). http://www.polytec.com
22. Safari, A., Akdogan, E.K.: Piezoelectric and Acoustic Materials for Transducer Applications. Springer, Berlin (2010)
23. Sashida, T., Kenjo, T.: An Introduction to Ultrasonic Motors. Oxford Science Publications, Oxford (1993)
24. Setter, N., Colla, E.L.: Ferroelectric Ceramics - Tutorial Reviews, Theory, Processing, and Applications. Birkhäuser, Basel (1993)
25. Smart Material GmbH: Manufacturer of piezoelectric composite actuators (2018). https://www.smart-material.com
26. Spanner, K.: Survey of the various operating principles of ultrasonic piezomotors. In: White Paper for Actuator, pp. 1–8 (2006)
27. Uchino, K.: Piezoelectric ultrasonic motors: overview. Smart Mater. Struct. **7**(3), 273–285 (1998)
28. Wallaschek, J.: Piezoelectric ultrasonic motors. J. Intell. Mater. Syst. Struct. **6**(1), 71–83 (1995)
29. Wallaschek, J.: Contact mechanics of piezoelectric ultrasonic motors. Smart Mater. Struct. **7**(3), 369–381 (1998)
30. Wallenhauer, C., Gottlieb, B., Kappel, A., Schwebel, T., Rucha, J., Lüth, T.: Accurate load detection based on a new piezoelectric drive principle employing phase-shift measurement. J. Microelectromech. Syst. **16**(2), 344–350 (2007)
31. Wang, Q.M., Cross, L.E.: A piezoelectric pseudoshear multilayer actuator. Appl. Phys. Lett. **72**(18), 2238–2240 (1998)
32. Weiß, M., Rupitsch, S.J.: Simulation-based homogenization and characterization approach for piezoelectric actuators. In: Proceedings of SENSOR and IRS2, pp. 415–419 (2017)
33. Weiß, M., Rupitsch, S.J., Lerch, R.: Homogenization and characterization of piezoelectric stack actuators by means of the inverse method. In: Proceedings of Joint IEEE International Symposium on the Applications of Ferroelectrics, European Conference on Application of Polar Dielectrics, and Piezoelectric Force Microscopy Workshop (ISAF/ECAPD/PFM), pp. 1–4 (2016)
34. Wolf, F.: Generalisiertes Preisach-Modell für die Simulation und Kompensation der Hysterese piezokeramischer Aktoren. Ph.D. thesis, Friedrich-Alexander-University Erlangen-Nuremberg (2014)

35. Wolf, F., Hirsch, H., Sutor, A., Rupitsch, S.J., Lerch, R.: Efficient compensation of nonlinear transfer characteristics for piezoceramic actuators. In: Proceedings of Joint IEEE International Symposium on Applications of Ferroelectric and Workshop on Piezoresponse Force Microscopy (ISAF-PFM), pp. 171–174 (2013)
36. Zhang, Z.M., An, Q., Li, J.W., Zhang, W.J.: Piezoelectric friction-inertia actuator - a critical review and future perspective. Int. J. Adv. Manuf. Technol. **62**(5–8), 669–685 (2012)
37. Zhao, C.: Ultrasonic Motors - Technologies and Applications. Springer, Berlin (2011)
38. Zhou, H., Henson, B.: Analysis of a diamond-shaped mechanical amplifier for a piezo actuator. Int. J. Adv. Manuf. Technol. **32**(1–2), 1–7 (2007)